HHS Public Access

Author manuscript

Bone. Author manuscript; available in PMC 2022 July 01.

Published in final edited form as:

Bone. 2021 July ; 148: 115962. doi:10.1016/j.bone.2021.115962.

Altered Collagen Chemical Compositional Structure in Osteopenic Women with Past Fractures: A Case-control Raman Spectroscopic Study

Gurjit S. Mandair[a,*], **Mohammed P. Akhter**[b], **Francis W. L. Esmonde-White**[c], **Joan M. Lappe**[b], **Susan P. Bare**[b], **William R Lloyd**[c], **Jason. P. Long**[d], **Jessica Lopez**[a], **Kenneth M. Kozloff**[d], **Robert R. Recker**[b], **Michael D. Morris**[c]

[a]School of Dentistry, Departments of Biologic and Materials, University of Michigan, Ann Arbor, Michigan, USA.

[b]Osteoporosis Research Center, Creighton University, Omaha, Nebraska, USA.

[c]Department of Chemistry, University of Michigan, Ann Arbor, Michigan, USA.

[d]Department of Orthopaedic Surgery, University of Michigan, Ann Arbor, Michigan, USA.

Abstract

Incidences of low-trauma fractures amongst osteopenic women may be related to changes in bone quality. In this blinded, prospective-controlled study, compositional and heterogeneity contributors of bone quality to fracture risk were examined. We hypothesize that Raman spectroscopy can differentiate between osteopenic women with one or more fractures (cases) from women without fractures (controls). This study involved the Raman spectroscopic analysis of cortical and cancellous bone composition using iliac crest biopsies obtained from 59-cases and 59-controls, matched for age (62.0±7.5 and 61.7±7.3 years, respectively, p=0.38) and hip bone mineral density

*Corresponding author: Gurjit S. Mandair, Department of Biologic and Materials Sciences, School of Dentistry, University of Michigan, Ann Arbor, MI 48109-1078, gmandair@umich.edu.

Authorship contributions

Study design and conception: MDM, JML, and RRR. Study conduct: GSM, MPA, JML, SPB, and RRR. Bone biopsy Raman data collection: GSM. Canine bone embedding: JPL. Canine bone Raman data collection: JL and GSM. Development of MATLAB code: FWLEW, GSM, and BRL. Data interpretation: GSM, MDM, and RRR. Writing the manuscript draft: GSM and MDM. Approval of final version of manuscript: All authors. Assurance of data integrity: GSM, MPA, MDM, and RRR.

CRediT authorship contribution statement

Gurjit S. Mandair: Investigation, Software, Formal analysis, Writing - Original Draft, Visualization. **Mohammed P. Akhter:** Conception, Investigation, Writing - Review & Editing. **Francis W. L. Esmonde-White:** Software. **Joan M. Lappe:** Conception, Investigation, Methodology, Writing - Review & Editing. **Susan P. Bare:** Investigation. **William R Lloyd:** Software. **Jason. P. Long:** Investigation, Resources. **Jessica Lopez:** Investigation, Formal analysis. **Kenneth M. Kozloff:** Writing - Review & Editing. **Robert R. Recker:** Conception, Investigation, Methodology, Funding acquisition, Writing - Review & Editing. **Michael D. Morris:** Conception, Methodology, Resources, Writing, Funding acquisition, Supervision, Writing - Review & Editing.

Conflict of interest

GSM, MPA, FWLEW, JML, SPB, WRL, JPL, and JL declare that they have no conflict of interest. MDM, RRR, and PAW have reported grants from National Institutes of Health, during the conduct of this study. MDM reports potential benefit as a result of the content being related to licensed technology to BioMatrix Photonics. KMK has received consultant fees from Mereo Biopharma and Ultragenyx Pharmaceuticals. KMK has received research funding from Cayman Chemical and Mereo Biopharma, and has received research supplies (sclerostin antibody) from Amgen Inc. and UCB.

(BMD, 0.827±0.083 and 0.823±0.072 g/cm^3, respectively, p=0.57). Based on aggregate univariate case-control and odds ratio based logistic regression analyses, we discovered two Raman ratiometric parameters that were predictive of past fracture risk. Specifically, 1244/1268 and 1044/959 cm^{-1} ratios, were identified as the most differential aspects of bone quality in cortical cases with odds ratios of 0.617 (0.406–0.938 95% CI, p=0.024) and 1.656 (1.083–2.534 95% CI, p=0.020), respectively. Both 1244/1268 and 1044/959 cm^{-1} ratios exhibited moderate sensitivity (59.3–64.4%) but low specificity (49.2–52.5%). These results suggest that the organization of mineralized collagen fibrils were significantly altered in cortical cases compared to controls. In contrast, compositional and heterogeneity parameters related to mineral/matrix ratios, *B*-type carbonate substitutions, and mineral crystallinity, were not significantly different between cases and controls. In conclusion, a key outcome of this study is the significant odds ratios obtained for two Raman parameters (1244/1268 and 1044/959 cm^{-1} ratios), which from a diagnostic perspective, may assist in the screening of osteopenic women with suspected low-trauma fractures. One important implication of these findings includes considering the possibility that changes in the organization of collagen compositional structure plays a far greater role in postmenopausal women with osteopenic fractures.

Keywords

Prospective study; Osteopenic women; Fracture risk; Raman spectroscopy; Bone quality; Bone composition

1. Introduction

Bone loss or osteopenia occurs when the rate of osteoclast-driven resorption exceeds the rate of osteoblast-dependent bone deposition [1]. This condition is accelerated in postmenopausal women as a result of reduced levels of estrogen, a hormone that promotes osteoblast activity and retards bone resorption by osteoclasts [2]. This hormonal imbalance eventually results in the overall reduction in bone mass and compromised bone architecture, such as reduced trabecular thickness, volume, connectivity, cortical thinning, and porosity [1]. The cumulative impact of these changes to bone increases the probability of fracture(s) occurring from low-trauma incidences, such as a fall from standing height or less [3].

Bone mineral density (BMD), as measured by dual energy X-ray absorptiometry (DXA), enables a diagnosis of osteopenia or the more severe osteoporosis to be made before the first fracture occurs. According to the World Health organization (WHO), osteoporosis is diagnosed by a *T*-score of −2.5 or lower and osteopenia with a *T*-score between −2.5 and −1.0 [4]. However, the prediction of fracture risk is complicated by the significant overlap in BMD values between individuals who have sustained a fracture from those who have not [5–7]. Fortunately, clinical researchers and basic scientists recognize several other properties that are also important predictors of fragility fractures, in addition to the widely used property of bone mass [8–10]. For instance, contributors to bone quality are related to the load-bearing functions of bone that include bone architecture and anisotropy at all length-scales, as well as tissue composition, and bone microdamage. Bone renewal is also required for the repair of bone microdamage and maintenance of bone architecture, and such

adaptation occurs through the process of bone remodeling [11]. The importance of bone quality components of bone architecture and composition to fracture risk prediction is still unclear [12, 13], although both are contributors.

To date, *ex vivo* techniques involving Fourier-Transform infrared (FTIR), nanoindentation, and backscattered electron microscopy have evaluated the contribution of bone quality and architecture to fracture risk in a multicenter prospective study [14–16]. The unique feature of these *ex vivo* studies is that the analyses were performed on (1) the same set of 120 iliac crest bone biopsies obtained from postmenopausal women with or without low-trauma fractures, and (2) biopsies from more challenging osteopenic patient population with *T*-scores between −2.5 and −1.0. However, Raman spectroscopy has yet to be evaluated under similar rigorous blinded, prospective-controlled study conditions.

Raman spectroscopy can be utilized as a confocal microscopy technique to analyze the molecular composition and heterogeneity of fresh or embedded bone specimens *ex vivo* [17–19] or as a non-invasive fiber-optic technique to analyze the composition of bone *in vivo* [20, 21]. Currently, Raman microscopy has been used to examine bone biopsies from postmenopausal women with osteoporosis [22, 23], osteoporotic women who have taken antiresorptive agents [24, 25], and experimental models of osteoporosis [26–29]. Raman spectroscopic measures of bone mineral and matrix quality include: mineral/matrix ratios, mineral crystallinity, *B*-type carbonate substitution [18, 30], apatitic mineral alignment [31], collagen crosslinks ratios [18, 29], collagen fibril organization [31, 32], and collagen post-translational modifications [33–36]. Furthermore, statistical heterogeneity outcomes associated with some of these spectroscopic parameters may also provide additional insights into bone turnover, but their relevance to fracture risk is still currently being debated [37–39].

In this blinded prospective study, Raman microscopy is used to evaluate the compositional and heterogeneity contributors of bone quality to fracture risk using iliac crest biopsies obtained from osteopenic postmenopausal women with one or more low-trauma fractures. We hypothesize that Raman microscopy can differentiate between women with fractures (cases, n=59) from women without fractures (controls, n=59) after controlling for age and BMD. In addition, we use logistic regression analyses to determine which of the Raman spectroscopic measures of bone quality contributes significantly to our ability to predict past fracture cases from controls.

2. Materials and methods

2.1. Study Participants and Biopsy Collection

In this blinded prospective study, 120 postmenopausal women with osteopenia were recruited by investigators at Creighton University [14]. Sixty women between 46 and 80 years, with a documented history of low BMD as measured by DXA (*T*-score between −2.5 and −1.0), and at least one low-trauma fracture were eligible for inclusion in the fracturing group (cases). Low-trauma fracture was defined as any fracture(s) caused by a fall to the floor from standing height or less [14]. Each fracturing woman (n=60 cases) was matched with a similarly aged woman (within 5 yrs) who had similar DXA bone measurements

(BMD within 10 % on hip), but without a fracture or a prior history of bone disease (n=60 controls). Biopsies were obtained within 5 years of fracture, but not less than 6 months after fracture [15]. None of the study participants demonstrated any disability or impaired mobility secondary to the fracture. The sample size of n=60 per group was calculated from power analyses performed on primary outcomes not examined in this study. More specifically, primary outcomes related to (1) histomorphometric activation frequency, (2) histomorphometric trabecular bone connectively density, and (3) nano-indentation hardness, with α = 0.05 (2-sided) and 80% power [15]. From the 120 biopsies collected, 118 were subsequently analyzed by Raman spectroscopy (n=59 cases and n=59 controls). Details of fracture types for cases are shown in Table 1. One case-control biopsy pair was excluded from the study because one of the biopsy exhibited extreme background fluorescence during Raman mapping. All study participants gave written informed consent for all procedures at Creighton University, including a biopsy collection. The study was approved by the Institutional Review Boards at Creighton University and the University of Michigan.

Transiliac bone biopsies were obtained using a Meunier's trephine with an inner diameter of 7.5 mm. Each bone core, intact with both cortical envelops and intervening cancellous bone, was defatted, dehydrated, and embedded in polymethylmethacrylate (PMMA) [40]. Embedded biopsies were sectioned and provided to study investigators without prior knowledge of the study participant's age or fracture status. The upper truncated embedded biopsy sections (Figure 1) were polished on wet silicon carbide paper of grit 400, 1200, and 4000 (Buehler, Lake Bluff, IL) with alumina slurry. After a final wet polish, the surfaces were imaged using a high-resolution CMOS camera (ThorLabs Inc., Newton, NJ). The external and internal sides of the two cortical envelops were not known and thus were given arbitrary thick cortex (Ct.A) or thin cortex (Ct.B) assignments (Figure 2).

2.2. Raman Microscopy, Mapping, and Calibration

The Raman microscope comprised of a epi-fluorescence microscope (Eclipse E600, Nikon Inc., Melville, NY) equipped with a 785 nm laser (Invictus, Kaiser Optical Systems Inc., Ann Arbor, MI) and X-Y stage (ProScan II, Prior Scientific Inc., Rockland, MA). Raman-scattered light was collected using an f/1.8 axial transmissive spectrograph (HoloSpec, Kaiser Optical Systems Inc.,) fitted with a 50-μm slit (6–8 cm^{-1} spectral resolution). A deep-depletion, back-thinned CCD camera (iDus, Andor Technology, Belfast, Northern Ireland, UK) with 1024 × 128 pixels was used (cooled to −75 ºC). The excitation laser was shaped into a line and the excitation light and spectral collection paths were made coaxial using a dichroic filter (LPD01–785RU, Semrock, Rochester, NY) [41]. The spectrograph was calibrated using a HoloLab Calibration Accessory (Kaiser Optical Systems Inc.,).

Raman maps were acquired using a 20x/0.75 *NA* objective (Nikon Inc.,) with ~100 mW at the biopsy. The laser line was always aligned perpendicular to the cortex to allow the greatest number of cortical structural features to be resolved by Raman microscopy (lateral resolution ~ 13 μm) (Figure 2). The length of the laser line was ~135 μm, yielding an interval spacing of ~1.1 μm per pixel. Each Raman transect was acquired using an optimized acquisition time of 1.5 mins. There were 22 transects in each cortical or cancellous Raman map to give a total mapping acquisition time of ~33 mins. For each cortex, three Raman

maps were collected from each of the three periosteal, mid-cortical, and endosteal regions in a systematic manner [42]. With a step-width of 10 μm, each cortical Raman map comprised of a mapping area of ~135 × 220 μm^2. Nine maps were acquired from each cortex with an acquisition time for ~33 mins per map. To ensure unbiased sampling, both osteonal and interstitial tissues were equally mapped. For cancellous bone, a variable step-width of 5–10 μm was used, yielding a mapping area between 135 × 110 μm^2 and 135 × 220 μm^2. Nine to twelve cancellous maps were acquired from the nodal and/or strut regions. A reference spectrum of pure PMMA was also acquired from each biopsy. All Raman mapping datasets, including neon, white light, Teflon, and dark calibration files were imported into MATLAB® Software (The MathWorks Inc., Natick, MA) for reprocessing and calibration [32, 41]. An automated spectral removal of PMMA interference from the mapping datasets was achieved using a derivative minimization algorithm [43], while an *„adaptive minmax'* polynomial fitting subroutine (3rd order, constrained) was used to correct for background tissue fluorescence [41]. All processed cortical and cancellous Raman maps were inspected individually and whenever necessary the outer boundaries were truncated to minimize interference from PMMA and/or spurious signals near the ends of the Raman laser line.

2.3. Bone Composition and Heterogeneity Analysis

Raman maps were created using custom-written MATLAB® scripts (The MathWorks Inc.,). The scripts applied a linear baseline correction to minimize local variations in background intensity (Figure S2). Raman intensity maps were created for the following bands and spectral ranges (shown in brackets): phosphate bands at ~959 cm^{-1} (ν_1PO_4, 950–970 cm^{-1}) and ~1044 cm^{-1} (ν_3PO_4, 1041–1048 cm^1); proline band at ~853 cm^{-1} (Pro, 850–860 cm^{-1}); average between proline and hydroxyproline bands at 853 and 873 cm^{-1}, respectively (Pro +Hyp, 848–875 cm^{-1}); phenylalanine band at ~1001 cm^{-1} (Phe, 999–1004 cm^{-1}); *B*-type carbonate band at ~1071 cm^{-1} (Carb, 1065–1073 cm^{-1}); amide III bands at ~1244 cm^{-1} (1240–1248 cm^{-1}) and ~1268 cm^{-1} (1264–1274 cm^{-1}); and amide I band at ~1667 cm^{-1} (1665–1678 cm^{-1}) (Figure S1). Four variants of the mineral/matrix ratio maps were then created: ν_1PO_4/Pro, ν_1PO_4/Phe, ν_1PO_4/(Pro+Hyp), and ν_1PO_4/Amide I [17, 44]. Relative *B*-type carbonate substitution in bone was calculated using Carb/ν_1PO_4 and Carb/Phe ratio maps [18, 23]. While 1044/959 and 1244/1268 cm^{-1} ratio maps provided structural information on the organization of apatitic mineral alignment or collagen fibril orientation, respectively [31, 32, 45]. Both 1044/959 and 1244/1268 cm^{-1} ratio maps may exhibit some polarization dependence due to the hierarchical organization (or anisotropic) nature of bone [32, 45, 46].

Four additional Raman parameters were obtained through curve-fit analysis. For each Raman map, 4–5 averaged spectra were created and imported into GRAMS/AI® Software (ThermoGalactic Inc., Salem, NH) for baselining, normalization and curve-fit analysis. No smoothing functions were applied to the Raman spectra. Mineral crystallinity was estimated from the full-width at half maximum (units of cm^{-1}) of the Gaussian-fitted ν_1PO_4 band at 959 cm^{-1} [32], with low values reflecting greater bone mineral crystal size and/or lattice perfection [19]. Hyp/Pro, Phe/(Pro+Hyp), and MMA/Pro+Hyp ratios were derived through curve-fit analysis of bands within 812–901 cm^{-1} (817, 837, 853, and 873 cm^{-1}) and 990–1010 (1001 cm^{-1}) spectral regions. Hyp/Pro and Phe/(Pro+Hyp) ratios were used as indirect

measures of collagen proline hydroxylation and collagen turnover, respectively [34, 35]. To indirectly assess the relative tissue water content (or nanoporosity), we used MMA/Pro+Hyp ratios, which was derived from the intensity ratio of the uncured residual polymer methylmethacrylate (MMA) band at ~837 cm^{-1} [47] to the sum of the bone collagen Pro and Hyp bands at ~853 and ~873 cm^{-1}, respectively. A high MMA/Pro+Hyp ratio value would reflect a greater degree of tissue water content (or nanoporosity) due to the greater infiltration of MMA into the tissue space (or pores) once occupied by water.

To assess the heterogeneity of the eight Raman mapping parameters, the datasets were imported into MATLAB® Software (The MathWorks Inc.,) and converted into pixel histograms using 50 equally sized bins. A mixed 2-Gaussian shape profile was fitted to each pixel histogram and the full-width at half-height (FWHM) value calculated. Narrow FWHM values would indicate a more uniform bone composition, while a wide value would indicate a more heterogeneous bone composition [15]. Mean FWHM values, including mean sample variance (SV) values, were calculated by averaging the results from all the cortical (Ct.A +Ct.B) and cancellous Raman maps. For the four curve-fit derived Raman parameters, only the mean SV cortical (Ct.A+Ct.B) and cancellous values were calculated.

2.4. Signal/Noise (S/N) Ratio Calculations

To determine the signal quality of Raman transects contained in each cortical Raman map, spectra were extracted over 1 or 100 pixels. Raw background-subtracted signal intensities for select Raman ν_3PO_4 (~1044 cm^{-1}), amide-III (~1245 and ~1269 cm^{-1}), and amide-I (~1667 cm^{-1}) bands were estimated in GRAMS/AI® software. Background room mean square (RMS) noise for each spectrum was calculated and averaged between the 1500–1540 and 1750–1850 cm^{-1} spectral ranges using the add-on RMS calculator in GRAMS/AI® software. The signal/noise (S/N) ratio was calculated by taking the ratio of the selected background-corrected signal intensity to the RMS noise [48]. Pixel spectra and S/N ratio calculations for select cortical Raman bands can be found in the supporting information section (Figure S2 and Table S1).

2.5. Specimen Orientation

The effects of specimen orientation on select 1244/1268 and 1044/959 cm^{-1} Raman parameters were illustrated in this study. For a single iliac crest bone biopsy specimen, Raman maps were taken with the Raman laser line being aligned perpendicular to the cortical envelop and then again in the parallel direction at the same approximate location [49]. Nine Raman maps were collected and analyzed for both thick (Ct.A) and thin (Ct.B) cortices using the procedures described in sub-sections 2.2 and 2.3.

2.6. Embedded Canine Bone Specimens

The effect of PMMA-embedding on select Raman band positions, intensities, and ratios were presented in this study. Canine bone specimens (n=2) were embedded in PMMA using the same protocol used to embed iliac crest bone biopsies examined in this multi-center study [40]. Details on canine bone specimens [50], embedding protocols, Raman mapping, and curve-fit analyses can be found in the supporting information section.

2.7. Statistical Analysis

Univariate case-control statistical comparisons were performed in SPSS Statistics Software for Windows (IBM SPSS Statistics Version 24, IBM Corp., NY). Mean Raman compositional and heterogeneity (FWHM and SV) values were evaluated. To assess the significant differences between cases (n=59) and controls (n=59), the non-parametric related-samples Wilcoxon signed rank statistical test was used (p<0.05) [14]. Logistic regression analysis was performed to identify which of the Raman parameter(s) that when combined with age, BMD, or age by BMD interaction variables, best predicted low-trauma bone fractures [14, 15]. A backward stepwise selection procedure was performed to eliminate parameters that did not contribute significantly to the models. The most significant explanatory parameters of the model(s) were identified, and Odds Ratios reported, together with 95% confidence intervals (CIs) and p-values. Only the reduced models (as opposed to the full models) were presented in this study due to the large number of compositional and heterogeneity parameters involved in this prospective study. Dot-scatter plots for select cortical and cancellous Raman parameters identified from the logistic regression analyses were created in Microsoft Excel Software. Standard deviations or 95% confident limits were added to the dot-scatter plots. Spaghetti plots were used to illustrate the relative change in select Raman band positions, intensities, and ratios between thawed and embedded canine bone specimens.

For each logistic regression model, raw true positive (TP), true negative (TN), false positive (FP), false negative (FN) numbers were also reported [51]. False positives were defined as study participants in the control group that were incorrectly classified as having a fracture, while false negatives were defined as study participants in the fracture group that were incorrectly classified as having no fractures. Percent sensitivity and specificity values were estimated as follows: Sensitivity (%) = TP / (TP + FN) x 100 % and specificity (%) = TN / (FP + FN) x 100 %.

3. Results

3.1. Study Characteristics

Table 1 shows the characteristics of the 118 enrolled postmenopausal women study participants, where the mean ages were 62.0 ± 7.5 years for the low-trauma osteopenic fracture group (cases, n=59) and 61.7 ± 7.3 years for the nonfracture osteopenic group (controls, n=59). There was no significant difference in age between the groups (p=0.38). Similarly, BMD and T-scores of the hip did not differ significantly between the groups (p = 0.57 and 0.59, respectively). The types of low-trauma fracture(s) for cases caused by falls from standing height or less are summarized in Table 1.

3.2. Analysis of Bone Composition by Fracture Status

Table 2 summarizes the results of the univariate case-control Raman spectroscopic analysis of cortical and cancellous bone composition. Among the twelve Raman spectroscopic parameters evaluated in this study, the only between-group significant differences were found in the bone matrix 1244/1268 cm^{-1} and mineral 1044/959 cm^{-1} ratio parameters. Dot-scatter plots showing the distributions and 95% confidence limits for the latter parameters

are illustrated in Figure S3 by bone type (cortical and cancellous) and experimental group (n=59 cases and n=59 controls). Similarly, Figure S4 shows the distributions and standard deviations between the thick cortex (Ct.A), thin cortex (Ct.B), and pooled result (Ct.A+B) by experimental group (n=59 cases and n=59 controls). Overall, 1244/1268 cm^{-1} ratios were significantly reduced in cortical and cancellous cases compared to their corresponding controls (1.043 ± 0.022 *vs.* 1.054 ± 0.025 with p = 0.0061, and 1.036 ± 0.025 *vs.* 1.045 ± 0.026 with p = 0.0154, respectively) (Table 1 and Figure S3). Whereas, 1044/959 cm^{-1} ratios were significantly increased in cortical cases compared to controls (0.143 ± 0.005 *vs.* 0.141 ± 0.006, p = 0.0242), but was borderline significantly increased in cancellous cases compared to controls (0.141 ± 0.006 *vs.* 1.139 ± 0.007, p = 0.0661) (Table 1 and Figure S3). A borderline increase in Hyp/Pro ratios was also found in cortical cases compared to controls (0.592 ± 0.046 *vs.* 0.582 ± 0.033, p = 0.0956). No significant differences were found using any of the other compositional parameters for either cortical or cancellous bone (Table 2).

3.3 Analysis of Bone Heterogeneity by Fracture Status

Table 3 shows the means of the sample variance (SV) calculated for each of the Raman compositional parameters shown in Table 2. Likewise, Table 4 shows the means of the FWHM measurements obtained from the pixel histograms of eight of the twelve Raman mapping parameters. Both SV and FWHM measurements were used to provide information on the degree of bone compositional variation (small *vs.* large) and heterogeneity (narrow *vs.* wide) for a given Raman parameter. Mean SV Hyp/Pro ratios were significantly increased in cortical cases compared to controls (1.954 ± 4.100 *vs.* 1.137 ± 1.577, divided by factor of 1000, p = 0.032), while mean SV MMA/(Pro+Hyp) ratios were borderline significantly increased in cancellous cases and compared to controls (0.261 ± 0.207 *vs.* 0.320 ± 0.243, divided by factor of 1000, p = 0.0709) (Table 3). No significant differences in cortical and cancellous SVs or FWHMs were found for any of the other Raman parameters shown in Tables 3 and 4, respectively.

3.4. Predictors of Past Fracture Risk by Logistic Regression Analysis

Logistic regression analysis was used to identify Raman parameters (Tables 2, 3, and 4) that significantly contributed to the prediction of fracture risk, with backward selection being used to eliminate all non-explanatory parameters (p > 0.05). As shown by the reduced models in Table 5, only two Raman compositional parameters were found to be significantly correlated with osteopenic fractures, namely, cortical 1244/1268 ratios (Model-1A, OR = 0.617, 95% CI 0.406–0.938, p=0.024) and cortical 1044/959 cm^{-1} ratios (Model-1B, OR = 1.656, 95% CI 1.083–2.534, p=0.020). Age and BMD variables, which were not significant predictors in themselves, were examined in each of the reduced models. No significant interactions between age or BMD with cortical 1244/1268 ratios (Model-2A, OR = 0.620, 95% CI 0.405–0.947, p=0.027) or cortical 1044/959 cm^{-1} ratios (Model-2B, OR = 1.697, 95% CI 1.095–2.632, p=0.018) were found, expect that the age interaction was almost significant in the latter model (p=0.0548).

As shown in Table 6, 21 and 24 false positives and 29 and 30 false negatives were incorrectly classified using cortical 1248/1268 (Model 1A) and 1044/959 cm^{-1} (Model 1B)

ratios, respectively. Adding age and BMD to the 1248/1268 cm^{-1} and 1044/959 cm^{-1} models, resulted in 21 and 22 false positives and 28 and 30 false negatives, respectively (Models 2A and 2B, respectively). Sensitivity of 64.4. 69.3, 64.4, 62.7 % and specificity of 50.8, 49.2, 52.5, 49.2 % were estimated for Models 1A, 1B, 2A, and 2B, respectively.

3.5. Signal Quality and Characteristics of Embedded Bone Raman Spectra

Figure S1a shows the appearance of a raw cancellous bone Raman spectrum (blue line, single transect) before and after applying the „*adaptive minmax'* polynomial fitting subroutine to correct for background tissue fluorescence (black line) and the derivative minimization algorithm to minimize spectral interference from cured PMMA (red line). The derivative minimization algorithm efficiently reduced spectral interference from minor PMMA 810 cm^{-1} and 1720 cm^{-1} bands near the bone matrix bands at ~852 cm^{-1} (proline) and ~1666 cm^{-1} (amide-I) bands, respectively. When compared to the reference spectra of PMMA and MMA (Figure S1b), embedded bone spectra (Figure S1a) contained two distinct Raman bands at ~835 and ~1638 cm^{-1}, which were attributed to uncured residual MMA. The derivative minimization algorithm only reduced spectral interference from PMMA and not MMA. Hence, bone Raman bands near ~593 (ν_4PO_4), ~1449 cm^{-1} (CH_2), and ~1638 cm^{-1} may contain residual spectral contributions from uncured MMA and thus are not used in any of our ratiometric Raman analyses. As shown by cortical Raman spectra in Figure S2, the signal intensities of all Raman bands taken over 1 or 100 pixels appeared to be uniform. Additionally, S/N ratios calculated for ν_3PO_4 (~1049 cm^{-1}) and amide-III (~1247 and ~1269 cm^{-1}) bands over a single pixel (S/N ratios of ~20.4, 18.4, and 17.5, respectively) were comparable to that of the strong amide-I (~1667 cm^{-1}) band (S/N ratio of ~20.0) (Table S1).

3.6. Effects of Specimen Orientation on 1244/1268 and 1044/959 cm^{-1} Parameters

Dot-scatter plots in Figure S5 illustrate the distributions of 1244/1268 and 1044/959 cm^{-1} ratio measurements taken from the thick (Ct.A) and thin (Ct.B) cortex with the Raman laser line being oriented parallel (∥) or perpendicular (⊥) to the cortical envelop. Distribution of the corresponding pooled cortical measurements (Ct.A+B) is also shown with standard deviations. For a given cortex, some specimen orientation bias was found using the 1244/1268 cm^{-1} parameter but less so when using the 1044/959 cm^{-1} parameter.

3.7. Effects of Embedding on Select Raman Parameters

Cortical Raman maps were acquired from the distal and proximal sides of two sectioned canine tibial bone blocks before and after embedding in PMMA (Figure S6). Figure S7 shows the representative site-matched Raman spectra of thawed bone and embedded bone. The latter spectra were baseline-corrected and normalized to the intensity of the amide III sub-band at ~1245 cm^{-1}. Based on curve-fit analyses, the effect of embedding on select Raman band positions, intensities, and ratios are summarized in Table S2, along with spaghetti plots in Figures S8 and S9, which illustrate how the amide I and amide III band positions shifted and ~1045/960 and ~1243/1268 cm^{-1} intensity ratios changed from thawed bone to embedded bone (Table S2). The shift in the amide III sub-band positions were small compared to the amide-I band position, which shifted by ~8 cm^{-1} to 1668 cm^{-1} (Table S2). As shown Table S2 and Figure S9, ~1045/960 ratio decreased slightly from 0.052 ± 0.005 to

0.045 ± 0.003 after embedding, while ~1243/1268 cm^{-1} ratio increased slightly from 1.14 ± 0.04 to 1.16 ± 0.04 after embedding.

4. Discussion

We hypothesize that Raman spectroscopy can detect differences in bone quality in age and BMD-matched iliac crest bone biopsies collected from osteopenic women with and without fractures. In this blinded, prospective-controlled study involving 118 postmenopausal women, three of the twelve Raman spectroscopic measures of bone quality were found to be significantly associated with low-trauma fractures (cases, n=59) compared to women without fractures (controls, n=59) (Tables 2–3). Based on case-control univariate analyses, the most significant outcomes were obtained using 1244/1268 cm^{-1}, 1044/959 cm^{-1}, and Hyp/Pro ratios. However, only 1244/1268 cm^{-1} and 1044/959 cm^{-1} ratios remained in subsequent logistic regression models (Table 5), and thus were identified as explanatory parameters of past fracture risk. The differential sensitivity of 1244/1268 cm^{-1} and 1044/959 cm^{-1} ratios to past fracture risk suggests that the organization of mineralized collagen fibrils were significantly altered in cases compared to controls.

Ratio variants of 1244/1268 cm^{-1} and 1044/959 cm^{-1} Raman parameters used in this current study had previously been used to spatially resolve the lamellae organization in Haversian bone as a function of orientation and location [31] using polarized Raman microscopy. Both 1271/1243 cm^{-1} and 1044/959 cm^{-1} ratios were strongest in lamellae nearest the Haversian canal, owing to the presence of more ordered mineralized collagen fibrils than those in the outermost lamellae. In essence, the relative intensity ratio between the bands at 1243 and 1271 cm^{-1} reflects the degree of orientation or anisotropy of collagen fibrils in bone. While no polarized Raman studies were performed in this study, we hypothesize that the low 1244/1268 cm^{-1} ratios found in cases were the result of changes to organization of collagen compositional structure within the lamellae of cortical and cancellous bone. Given that apatitic mineral is usually aligned parallel to the collagen fibrils may explain why 1044/959 cm^{-1} ratios were reciprocally increased in cases compared to controls. Although, the low resolution of our Raman maps precluded any detailed spatial study of lamellar bone, a small subset of biopsies, the same ones used in this study, were recently analyzed by circularly polarized light (CPL) microscopy [52]. In the latter study, the width of *extinct* and *bright* lamellae in cortical bone were reported to be significantly reduced in fracturing patients (cases, n=8) compared to non-fracturing patients (controls, n=8). More importantly, cortical bones from fracturing patients were also reported to display fewer *extinct* lamella birefringents compared to non-fracturing patients. Birefringence signals in CPL correspond to a specific collagen arrangement, with *extinct* lamella comprising of mainly collagen forming small angles with respect to the general orientation of the Haversian system. Fewer *extinct* lamellae would in part support our hypothesis of the involvement of altered mineralized collagen fibril organization in fracture cases.

In logistic regression analyses, 1244/1268 and 1044/959 cm^{-1} ratios were identified as explanatory parameters of past fractures for cortical bone (Table 5). In detail, a one-unit decrease in cortical 1244/1268 ratio (Model-2A) and a one-unit increase in cortical 1044/959 cm^{-1} ratio (Model-2B) were associated with 38% decrease and 34% increase odds

of fracture, respectively. Both these explanatory parameters were negatively intercorrelated with each other, meaning that if one parameter appeared in the model, then the other parameter would not significantly add to the model. It is noteworthy that these explanatory parameters were different to the variables identified in the parallel Fourier-transform infrared (FTIR) imaging study using the same set of bone biopsies [15]. In the latter study, carbonate/phosphate ratios and/or collagen maturity heterogeneity variables were identified as significant predictors of past fracture risk from conditional logistic regression analyses in cortical and cancellous bone.

To put the predictive performance of cortical 1244/1268 and 1044/959 cm^{-1} ratios of past low-trauma fracture(s) into perspective, we also examined the number of false positives and negatives, sensitivity, and specificity. When considering cortical 1244/1268 and 1044/959 cm^{-1} ratios alone or in combination with age and BMD, the final logistic regression models identified 21–24 false positives and 28–30 false negatives (Table 6). Accordingly, both cortical 1244/1268 and 1044/959 cm^{-1} ratios exhibited moderate sensitivity (59.3–64.4 %) but low specificity (49.2–52.5%). From a clinical perspective, this would mean that some osteopenic women who have not sustained a fracture may be incorrectly classified as having a fracture (false negative) and thus would need to undergo further evaluation.

The salient finding of altered 1244/1268 and 1044/959 cm^{-1} ratios in women with fractures in this study may have clinical relevance in understanding the role of bone anisotropy in osteoporosis and falls. There is evidence that the anisotropy of trabecular bone in the vertebra of osteoporotic patients [53] and femora of hip-fracture patients [7, 54] are strongly orientated with the loading direction. Increased bone anisotropy is reported to compensate for low bone mass to ensure adequate bone stiffness or strength in the frequently of the loaded direction. Consequently, osteoporotic patients with increased vertebral anisotropy are at higher risk of failure due to uncommon “error” loads, such as forward flexion or lifting; while hip patients with increased femoral anisotropy would be less likely to withstand “off-axis” impacts, such as a sideways fall [7, 55]. Both 1244/1268 and 1044/959 cm^{-1} ratios also partially reflect the anisotropic character of bone, which leads us to suggest that the cases contained more orientated mineralized collagen fibrils than the controls. However, information on fall direction were not collected in this study and that only two cases sustained a hip fracture, while the majority of fractures occurred at the wrist, vertebra, and ankle locations [14]. While there is a possibility that study participants in the fracture group may have had a greater propensity to fall, study participants in both groups were (1) healthy individuals since the exclusion criteria ruled out those with many major disorders, and (2) were matched for age, which is itself a risk factor for falls [56].

The reason why 1045/959 cm^{-1} ratio increased in cases compared to controls requires further discussion, but first we discuss why the 1244/1268 cm^{-1} ratio did not increase in cases compared to controls. Cortical 1245/1270 cm^{-1} ratio has been reported to increase in bovine bone after thermal denaturation and to a lesser extent after mechanical denaturation [57]. Thermal and mechanical denaturation was reported to perturb collagen secondary structure, with a transition from ordered to less-ordered helical structure. In two independent osteoarthritis studies, cartilage 1241/1269 cm^{-1} or 1245/1270 cm^{-1} ratio was reported to increase with severity of disease progression, as assessed by the Kellgren-Lawrence (0–5

grade scale) or International Cartilage Repair Society (grades I-III) scoring systems, respectively [58, 59]. High scores were associated with greater relative content of less-ordered forms of collagen secondary structure. Similar interpretations have also been used to describe changes in ocular tissues from a transgenic mouse model of osteoarthritis [60] and muscle tissues from patients with mature heterotopic ossification [61]. Given that 1244/1268 cm^{-1} ratio was found to be lower in cases compared to controls in the current study suggests that they contained more ordered collagen helical structure. This reasoning would be in line with a recent osteogenic cell culture study [62], whereby 1246/1264 cm^{-1} ratios declined steady over a 28-day period, owing to the progressive coalignment between collagen fibrils and apatitic mineral crystallites. Similarly, mid-cortical 1246/1269 cm^{-1} ratio was reported to decline with age in the radii from male donors (n=37, 18 to 89 years of age) [63]. However, study participants involved in the current study were matched for age and thus an alternative explanation (other than age effects) is required to explain why 1244/1268 cm^{-1} ratio decreased in cases compared to controls.

In regards to the 1044/959 cm^{-1} parameter, a Raman spectroscopic study performed on tooth enamel reported that the 1043/959 cm^{-1} ratio was elevated in intact sound enamel surfaces compared to sectioned sound enamel [64]. This result showed that conventional Raman spectroscopy was capable of detecting relative hierarchical organizational differences in enamel lamellae without the need for specialized polarized Raman optics. At least for the carious lesion, the latter ratio did not appear to be sensitive to polarized Raman direction and was higher compared to surrounding sound enamel. The authors of the latter study associated elevated 1044/959 cm^{-1} ratios to increased scrambling of the orientation of enamel crystallites due to demineralization effects. However, Raman mineral/matrix ratios were not significantly different between cases and controls in the current study, and thus an alternative explanation is required to explain why 1044/959 cm^{-1} ratios increased in cases compared to controls.

Given that variants of 1244/1268 cm^{-1} and 1045/959 cm^{-1} ratios have been reported to be dependent on the organization of mineral or collagen fibrils in cortical bone, dental, and/or muscle tissues, as assessed by conventional or polarized Raman spectroscopies [31, 45, 61, 63, 64], suggests that the orientation of mineralized collagen fibrils were altered in cases compared to controls. This reasoning is also indirectly supported by other studies, whereby the impact of bone pathologies and therapies on the orientation of collagen and/or biological apatite (Bap) were investigated. First, in an ovariectomized (OVX) rat model of osteoporosis, the *c*-axis orientation of biological apatite (Bap) from the vertebra was significantly higher in the OVX group compared to the Sham group, indicating an increase in the anisotropy in the material parameter [65]. More importantly, the high Bap *c*-axis orientation in the OVX group recovered after administration of Risedronate or combined Alfacalcidol and Risedronate treatments for 12-weeks. Second, Raman measures of bone quality and Bap preferential *c*-axis orientation were altered in a rat model of chronic kidney injury [66]. Both Bap *c*-axis orientation and Raman measure of pentosidine/matrix ratio were identified as significant determinants of elastic bone material strength. Impaired mechanical function has also been reported in a rodent model of osteoblastic bone metastasis, where the preferential alignment of both collagen and Bap in PCa-bearing long bones was disrupted [67]. Third, lamellae thickness and lamellae birefringence in the

Haversian system of iliac crest biopsies obtained from postmenopausal women were reported to improve after treatment with parathyroid hormone (PTH) for 36 months [68]. It was proposed that increased lamellar thickness following PTH treatment altered the distribution of birefringence and therefore the distribution of collagen orientation. Fourth, *extinct* and *bright* lamellae width were also reported to be reduced by 8% and 5% in iliac crest biopsies from fracturing patients compared to non-fracturing patients [52]. However, it is unclear whether changes in lamellae width could also help explain why 1244/1268 cm^{-1} ratio decreased and 1044/959 cm^{-1} ratio increased in cases in the current study. This requires further investigation. Notwithstanding, a recent FTIR and nano-indentation study showed that *bright* and *dark* osteon types in femoral human bone exhibit distinct local compositional profiles that reflected their local mechanical environment [69].

In regards to a biological rationale into why lamellae width and birefringence were reduced in fracturing patients, it was recently hypothesized that certain genes related to osteoblast Wnt signaling participate in establishing collagen orientation in bone [52]. Wnt signaling is also known to be active during bone fracture repair [70–72] and cooperates with other systemic bone growth regulators (e.g. PTH) [73], while its mutation or deletion is associated with some rare forms of osteoporosis [74, 75]. Changes in Wnt signaling patterns could, hypothetically, explain why Raman measures of 1244/1268 and 1044/959 cm^{-1} ratios were significantly altered in cases compared to controls in this current study. Although, Wnt signaling was not assessed in this current study, it has been shown to indirectly impact Raman spectra and Raman compositional measures of bone quality in experimental models of aortic value calcification [76], osteocyte mineralization [77], lead exposure [78], tooth damage [79], and bisphosphonate-induced osteonecrosis [80].

In regard to Raman Carb/ν_1PO_4 ratios, a measure of the amount of *B*-type carbonate substitution for phosphate ions in apatitic mineral, no significant differences were found between cases and controls for either cortical or cancellous bone (Table 2). This contrast with the significant outcome reported in the previous Raman imaging study [23], whereby cortical Carb/ν_1PO_4 ratios were increased in iliac crest bone biopsies from women with osteoporotic fractures (n=14) when compared to women without fractures (n=8). Although, comparative *s*tudies between osteopenic and osteoporotic patient populations are limited or underpowered, some differences in bone quality and microarchitectural properties have been reported [81–83]. The contradictory Carb/ν_1PO_4 ratio outcomes obtained between these Raman spectroscopic studies could be the result of analyzing biopsies from two different patient populations, with osteopenic patients perhaps displaying a different turnover phenotype than osteoporotic patients. However, the contrasting FTIR carbonate/phosphate [15] and Raman Carb/ν_1PO_4 ratio (this study) outcomes obtained from the same case-controlled study could be attributed to instrumental differences.

The absence of significant mineral crystallinity differences between cases and controls in this study (Table 2) echoes the similar non-significant crystallinity outcomes reported by the parallel FTIR imaging study [15]. At least from our Raman spectroscopic perspective, osteopenic fractures were not strongly associated with changes in mineral crystal size and/or lattice perfection [84]. The non-significant outcome of the corresponding Raman Carb/ν_1PO_4 ratios (Table 2) would support this argument as the latter parameter is known to be

reciprocally correlated with changes in the mineral crystallinity parameter [30]. Moreover, *in vitro* and *ex vivo* spectroscopic studies performed on murine models of bone development have shown that mineral crystallinity rapidly reaches a plateau during early bone growth, while mineral/matrix ratios may continue to increase linearly with time [85, 86]. A similar pattern has also been reported in iliac trabecular bone biopsies from pediatric patients [87]. However, the spatial assessment of mineral crystallinity by bone surface was not examined in this study. As such, averaging mineral crystallinity measurements from all cortical bone surfaces (periosteal, mid-cortical, bone and endosteal bone) may have masked any underlying spatial differences due to bone remodeling.

The measurement of mineralization in bone is recognized as the mainstay of bone quality assessments. In Raman spectroscopy, mineralization assessments are based on mineral/matrix ratios, which have been correlated with ash content [44], Calcium mass fraction [88], or tissue mineral density [89], including being validated against synthetic bio-apatitic standards [90]. However, there is still no agreed upon consensus on which variant of the Raman mineral/matrix ratio(s) should be used to evaluate fractures as each variant has its own unique strengths and weaknesses in terms of practicality, sensitivity, and polarizability [17, 44, 91]. In this study, four variants of the following mineral/matrix ratios, based on the normalized intensity of the ν_1PO_4 band at ~959 cm^{-1}, were examined: ν_1PO_4/Amide I, ν_1PO_4/Pro+Hyp, ν_1PO_4/Pro, and ν_1PO_4/Phe ratios (Table 2). Regardless of the mineral/matrix ratio used, no significant differences between cases and controls were found for either cortical or cancellous bone. The lack of any significant differences in mineral/matrix ratios was not entirely unexpected given that the study was designed to control for BMD (within 10% on hip) and to ensure that only statistical differences associated with low-trauma fractures were identified. Similar non-significant mineral/matrix ratios and degree of mineralization of bone (DBM) outcomes have been reported by parallel FTIR imaging [15] and quantitative digitized microradiography [16] studies, respectively. Furthermore, mineralization assessments based on Raman ν_4PO_4/Amide III ratios have also recently been performed on a small sub-set of biopsies [92]. The latter parameter was considered less sensitive to the intrinsic orientation (or polarization) of mineralized collagen fibrils in bone [91]. The ν_4PO_4/Amide III ratio was not found to be significantly different between cases (n=6) and controls (n=6) for either cortical or cancellous bone [92].

Collectively, the lack of compositional differences in mineral crystallinity, carbonate substitution, or mineral/matrix ratios in the current study could also be attributed to measurements not taken at the actual fracture site. In a previous study, Raman measurements were taken at the damaged region and 2-mm away in femoral specimens obtained from postmenopausal women who had sustained fracture(s). Trabecular carbonate/phosphate, phosphate/amide-I, and carbonate/amide-I ratios were reported to be borderline different at the damaged region compared to 2-mm away. In the same publication, cortical carbonate/phosphate ratios were found to be significantly higher in iliac crest biopsies obtained from postmenopausal women who have sustained fracture(s) compared to those women who had not, despite the fracture location being far-removed i.e. within the femora and vertebra. Although, not appreciated at the time, both phenomena speak to possible regional and systemic effects of fracture(s) on bone quality, respectively [93, 94]. While the impact of systematic changes to bone composition remains to be investigated, skeletal fracture may

initiate systematic changes in bone quantity, which in turn increase the risk of fracture at all skeletal sites.

Although not statistically significant, Hyp/Pro ratios were found to be marginally elevated in cortical cases compared to controls (Table 2). Such elevations could reflect increased intra-strand stability of the collagen triple helix or increased post-translational hydroxylation of proline residues in collagen [34, 35]. While bone and urinary hydroxyproline levels have frequently been used as biomarkers of bone remodeling in postmenopausal women with osteoporosis [95–97], the Hyp/Pro ratio used in this study was not calibrated to provide an absolute measure of proline hydroxylation. Alternatively, the marginal increase in Hyp/Pro ratio could be attributed to indirect effects that are not related to post-translational modifications but to changes in collagen secondary structure. In a recent *in vitro* glycation study [36], Raman Hyp/Pro ratios were increased in glycated human cortical bone due to the accumulation of advanced-glycation endproducts (AGEs). It was proposed that collagen molecules in glycated bone samples may have undergone a supra-molecular rearrangement, whereby the intensity of the hydroxyproline band became more Raman sensitive compared to the intensity of the adjacent proline band. Such an effect could account for the marginal increase in Hyp/Pro ratios found in cortical cases in this study. Although, the accumulation of AGEs have been linked to osteoporosis [98] and proposed by other co-authors involved in this multicenter study [92], additional blinded studies will be needed to determine their relevance to osteopenic women with low-trauma fractures.

Statistical measures of compositional heterogeneity (FWHM) and sample variance (SV) were also examined in this study. Although the contribution of heterogeneity measures to fracture risk is currently being debated [37–39], the loss of compositional or material heterogeneity is often associated with reduced bone remodeling or diminished material properties. Despite the non-significant outcomes of all eight Raman mapping FWHM and SV parameters (Tables 4 and 3), one significant and one borderline significant SV outcome was identified in two of the four peak-fitted Raman parameters (Table 3). More specifically, cortical SV Hyp/Pro ratios were significantly higher i.e. more heterogeneous in cases compared to controls, with collagen molecules at various stages of supra-molecular rearrangement. In contrast, cancellous SV MMA/(Pro+Hyp) ratios were marginally lower in cases compared to controls (Table 3). In our study, the MMA/(Pro+Hyp) ratio was a variant of the surrogate PMMA/amide III ratio used [99, 100] to indirectly assess tissue water content (or nanoporosity) of bone at the sub-micron level. The use of MMA/(Pro+Hyp) ratio was necessary because an algorithm was used to remove spectral interference from cured PMMA but not of residual uncured MMA, which was represented by a distinct minor Raman band at ~835 cm^{-1} [47]. As a compositional measure, increased MMA/(Pro+Hyp) ratio would reflect a greater infiltration of uncured MMA into tissue spaces that was once occupied by water. We propose that the narrow water distribution found in cancellous cases was related to the inability of collagen to properly interact or bind water, but this requires further validation. Notwithstanding, increased cross-linking in connective tissues have been reported to impair the ability of collagen to bind water [101].

Despite some evidence for altered matrix heterogeneity in this cohort of osteopenic women with low-trauma fracture(s), mineral heterogeneity FWHM and SV assessments were

unremarkable (Tables 4 and 3). Non-significant FTIR mineral/matrix heterogeneity and DBM heterogeneity index outcomes were also reported on the same set of biopsies [15, 16]. Interesting, in parallel nanoindentation heterogeneity assessments performed on second biopsy specimens [14], fracturing women (n=60) consistently displayed reduced SV hardness and/or modulus than non-fracturing women (n=60). The different Raman and nanoindentation SV outcomes could be attributed to where the measurements were made. In nanoindentation, cortical indent sites were localized to interstitial tissues, while both cortical interstitial and osteonal tissues were mapped by Raman spectroscopy. Although, nanoindentation and Raman mapping were localized to the center of each trabeculae, the spatial area probed by the latter technique was considerably larger. Averaging Raman mapping datasets together without first parsing out bone microstructural features may have also obscured some of the more localized mineral heterogeneity differences. The importance of spatially localized Raman spectroscopic and nanoindentation measurements were recently highlighted [102], whereby unresorbed osteons in human bone were reported to be more heterogeneous compared to resorbed osteons. Similarly, parallel FTIR and nano-indentation studies performed on *dark* and *bright* osteons demonstrated the coupling of localized compositional and mechanical properties [69]. More specifically, *dark* osteons with their longitudinally oriented collagen fibers and high mineral/matrix ratios and mean calcium content conferred higher stiffness, while *bright* osteons with their oblique-angled collagen fibers provided more ductility and ability to dissipate energy more efficiently. Furthermore, the time-lag of up to 5 years between the occurrence of low-trauma fracture(s) and the biopsy collection may have allowed bone remodeling enough time to change mineral heterogeneity post-fracture.

Embedding effects on key Raman 1244/1268 and 1044/959 cm^{-1} parameters identified in this study also need to be discussed. Studies have shown that dehydrating or embedding bone tissues may impact bone compositional and structural outcomes determined by Raman spectroscopy [49, 103]. While collagen fibrils in bone tissues may shrink due to solvent dehydration or embedding, their hierarchical organization is expected to be largely preserved, and thus possible to still obtain relative structural and compositional information between experimental groups. In early polarized Raman imaging studies performed on human bone, the orientation of the osteonal lamellae amide I and III images were resolvable, despite the tissues being fixed in ethanol and embedded in PMMA [91]. In a correlative study, cortical Raman ν_2PO_4/amide III ratios were found to be correlated with calcium content, despite the tissues being dehydrated in ethanol and embedded in PMMA [88]. All 118 bone biopsies used in the current study were dehydrated, defatted, and embedded in PMMA in the same way, and thus any compositional or structural differences between cases and controls is expected to be relative. Additionally, supplemental data on the embedding effects on select bone Raman band positions, intensities, and/or ratios related to 959, 1044, 1244, 1268, 1662 cm^{-1} bands were provided in this study using canine bone specimens. The shift in the amide III sub-band positions (Figures S7-8 and Table S2) after embedding canine cortical bone in PMMA was not as dramatic as compared to the amide-I band position, which shifted by ~8 cm^{-1} to 1668 cm^{-1}. At the molecular level, ν(C-N) and δ(N-H) bonds associated with the amide III sub-bands appeared to be less affected by embedding in PMMA compared to the amide-I carbonyl ν(C=O) bonds. Similarly, canine cortical

~1045/960 ratios decreased slightly from 0.052 ± 0.005 to 0.045 ± 0.003 upon embedding, while cortical ~1243/1268 cm^{-1} ratios increased slightly from 1.14 ± 0.04 to 1.16 ± 0.04 upon embedding (Table S2 and Figure S8). At least for the key 1244/1268 cm^{-1} ratio metric used to analyze iliac crest bone biopsies, embedding effects appeared to be small compared to thermal denaturation effects reported recently for bovine bone. In more detail, Raman 1245/1270 cm^{-1} ratio was reported to increase from 1.050 ± 0.028 to 1.179 ± 0.076 after cortical bone was boiled in water for 90–120 mins [104]. Interestingly, a recent CPL study found that corresponding *extinct* and *bright* lamellae width were reduced by 8% and 5% in iliac crest bone biopsies from fracturing patients compared to non-fracturing patients [52]. The latter biopsies were embedded in the same way as the biopsies analyzed by Raman mapping in the current study and by FTIR imaging in the previous parallel study [15]. While fresh tissues are often preferred for spectroscopic analyses, the use of embedded specimens is an acceptable alternative given the design of the multi-center study.

Certain bone Raman bands used in ratio parameter calculations are known to exhibit some specimen orientation bias [49]. To minimize such biases, it has been recommended that the Raman laser should always be aligned transversely or longitudinally with respect to the specimen surface. Given that cortical 1044/959 and 1244/1268 cm^{-1} ratios may exhibit some orientation bias, a similar laser-specimen orientation control experiment was performed in this study. For a single biopsy, compositional maps were taken with the Raman laser line aligned perpendicular to the thick (Ct.A) and thin (Ct.B) cortices before the specimen was rotated by 90° to allow Raman maps to be taken in the parallel direction at the same location. The slight differences in mean 1044/959 and 1244/1268 cm^{-1} ratio values obtained between Ct.A and Ct.B for a given laser orientation could be attributed to differences in bone morphology, with one cortex perhaps containing more lamellae bone compared to the other cortex [42, 105]. As expected, 1044/959 and 1244/1268 cm^{-1} ratios exhibited some orientation bias (Figure S5). For this reason, the Raman laser line was always aligned perpendicular to the surface at each cortex for all of the 118 biopsies analyzed in this study (Figure 2). Moreover, the distribution of all 1044/959 and 1244/1268 cm^{-1} ratio data points were not skewed in one cortex over the other (Ct.A *vs.* Ct.B, n=59 per group) and that they varied consistently between cases and controls (Figure S4). Reporting averaged cortical (Ct.A+Ct.B) 1044/959 and 1244/1268 cm^{-1} ratio values for each biopsy specimen may have also helped further minimize any specimen orientation bias.

5. Strengths, limitations, and conclusions

A number of strengths and limitations of this study may be considered. The strengths of this study include the prospective design to control for participant study age and BMD; biopsy collection from a representative and relatively large osteopenic population; and blinding of the fracture status to the study investigators. However, this study has some limitations, some of which have already been addressed by other investigators involved in this multicenter study [14–16].

One potential limitation of this study is that biopsies were collected from osteopenic women who had sustained low-trauma fracture within a 5 year period, but not less than 6-months after the fracture. It is possible that for some biopsies, significant bone remodeling may have

occurred over this time period. However, all study participants were at least 4-years postmenopausal and thus their rate of bone remodeling was expected to be low. Additionally, study participants were excluded from the study if they were on any medications that may have affected bone remodeling.

While Raman spectroscopic measures of 1244/1268 and 1044/959 cm^{-1} ratios were found to contain hierarchical organizational information that were predictive of past fracture risk, they were not calibrated to provide absolute measures of the preferred orientation of collagen fibrils or the angular distribution of the mineralized collagen lamella between cases and controls. Such information could be obtained using polarized Raman microscopy, but was not considered in our original study design. A recent polarized Raman microscopy study found that mineral-crystal orientation oscillated between each lamella up to 35-μm away from the Haversian canal [31]. It follows that the intensity ratio of the 1240/1270 and 1046/960 cm^{-1} parameters used in the latter study would oscillate between each lamella multiple times before reaching the outermost lamella. While our 1244/1268 and 1044/959 cm^{-1} ratio Raman maps were broadly featureless, they would have been large enough (~100 × 220 μm^2 area after truncation) to have sampled over multiple lamellae. It is only through statistical analyses that subtle differences in our cortical 1244/1268 and 1044/959 cm^{-1} ratio parameters became apparent between cases and controls. Unlike for cortical bone, the orientation of the Raman laser line with respect to the trabecular surface could not be controlled because of its more complex and varied lamellar organization. However, univariate case-control analyses show that cancellous 1244/1268 and 1044/959 cm^{-1} ratios tracked in the same direction as that for cortical bone.

Spectroscopic measures of Hyp/Pro ratios provided some insights into collagen quality, but additional validation studies are still necessary. Clarification is still needed to determine whether Hyp/Pro ratio measures reflect changes in post-translational collagen modifications (e.g. proline hydroxylation) or collagen secondary structure (e.g. supra-molecular rearrangement due to formation in AGEs). If they reflect the former, then Hyp/Pro ratios should be correlated with HPLC measures of bone Hyp/Pro content. Similar validation studies are also necessary for our proposed MMA/(Pro+Hyp) ratio parameter, which was used in this study as an indirect measure of bone water content. The importance of water content to bone quality has already been highlighted indirectly in embedded bone specimens [99, 100] and directly in fresh bone specimens [57, 106]. The bone biopsies used in this study were already embedded and our Raman microscope was only equipped with a low wavenumber grating. Thus, a direct and indirect spectroscopic comparison of bone water content was not possible in this study. This requires further investigation.

In conclusion, the outcomes of this blinded prospective study in part support our hypothesis that Raman spectroscopy can detect changes to bone quality in osteopenic women with low-trauma fractures. Based on aggregate univariate case-control and logistic regression analyses, 1244/1268 and 1044/959 cm^{-1} ratios were found to be the most differential aspects of bone quality in cortical cases compared to controls. In contrast, compositional and associated heterogeneity measures of bone quality, namely mineral/matrix ratios, *B*-type carbonate substitution, and mineral crystallinity, were not significantly different between cases and controls. Taken together, our study highlights the importance of analyzing the

organization of collagen compositional structure when evaluating postmenopausal women with suspected low-trauma osteopenic fractures. Future studies will be aimed at improving both sensitivity and specificity of our logistic regression models by inclusion of other variables identified in parallel FTIR [15] and nano-indentation [14] studies.

Supplementary Material

Refer to Web version on PubMed Central for supplementary material.

Acknowledgements

This study was supported by grant R01-AR054496 from the National Institute of Arthritis and Musculoskeletal and Skin Diseases (NIAMS). GSM also acknowledges partial support by NIH grant P30 AR069620 (Karl J. Jepsen, PI; David H. Kohn, Core Director of the Michigan Integrative Musculoskeletal Health Core Center or MiMHC). All authors thank Dr. Patrice A. Watson (Creighton University) for her statistical support. GSM and MDM also thank Center for Statistical Consultation and Research (CSCAR) of the University of Michigan for statistical support. GSM and MDM thank Dr. Steven Goldstein (University of Michigan) for useful discussions. The authors thank all the study participants who provided bone biopsies for this study.

References

[1]. Armas LAG, Recker RR, Pathophysiology of osteoporosis: New mechanistic insights, Endocrinol. Metab. Clin. North. Am 41 (2012) 475–486, 10.1016/j.ecl.2012.04.006. [PubMed: 22877425]

[2]. Riggs BL, Khosla S, Melton LJ, Sex steroids and the construction and conservation of the adult skeleton, 23 (2002) 279–302, 10.1210/er.23.3.279.

[3]. Deloumeau A, Molto A, Roux C, Briot K, Determinants of short term fracture risk in patients with a recent history of low-trauma non-vertebral fracture, Bone 105 (2017) 287–291, 10.1016/j.bone.2017.08.018. [PubMed: 28842362]

[4]. Kanis JA, Alexeeva L, Bonjour JP, Burkhardt P, Christiansen C, Cooper C, Delmas P, Johnell O, Johnston C, Khaltaev N, Lips P, Mazzuoli G, Melton LJ, Meunier P, Seeman E, Stepan J, Tosteson A, Assessment of fracture risk and its application to screening for postmenopausal osteoporosis: synopsis of a WHO report. WHO Study Group, Osteoporosis Int. 4 (1994) 368–381, 10.1007/bf01622200.

[5]. Cummings SR, Are patients with hip fractures more osteoporotic? Review of the evidence, Am. J. Med 78 (1985) 487–494, 10.1016/0002-9343(85)90343-2. [PubMed: 3976707]

[6]. Riggs BL, Wahner HW, Dunn WL, Mazess RB, Offord KP, Melton LJ, Differential changes in bone mineral density of the appendicular and axial skeleton with aging: relationship to spinal osteoporosis, J. Clin. Invest 67 (1981) 328–335, 10.1172/jci110039. [PubMed: 7462421]

[7]. Ciarelli TE, Fyhrie DP, Schaffler MB, Goldstein SA, Variations in three-dimensional cancellous bone architecture of the proximal femur in female hip fractures and in controls, J. Bone Miner. Res 15 (2000) 32–40, 10.1359/jbmr.2000.15.1.32. [PubMed: 10646112]

[8]. Hernandez CJ, Keaveny TM, A biomechanical perspective on bone quality, Bone 39 (2006) 11731181, 10.1016/j.bone.2006.06.001.

[9]. Donnelly E, Methods for assessing bone quality: A review, Clin. Orthop. Relat. Res 469 (2011) 2128–2138, 10.1007/s11999-010-1702-0. [PubMed: 21116752]

[10]. Nakano T, Advances in Metallic Biomaterials: Tissues, Materials and Biological Reactions, Springer-Verlag Berlin and Heidelberg GmbH & Co. KG, Berlin, Germany, 2015.

[11]. Clarke B, Normal bone anatomy and physiology, Clin. J. Am. Soc. Nephrol 3 (2008) S131–S139, 10.2215/cjn.04151206. [PubMed: 18988698]

[12]. Donnelly E, Lane JM, Boskey AL, Research perspectives: The 2013 AAOS/ORS Research Symposium on bone quality and fracture prevention, J. Orthop. Res 32 (2014) 855–864, 10.1002/jor.22626. [PubMed: 24700449]

[13]. Cefalu CA, Is bone mineral density predictive of fracture risk reduction?, Curr. Med. Res. Opin 20 (2004) 341–349, 10.1185/030079903125003062. [PubMed: 15025843]

[14]. Vennin S, Desyatova A, Turner JA, Watson PA, Lappe JM, Recker RR, Akhter MP, Intrinsic material property differences in bone tissue from patients suffering low-trauma osteoporotic fractures, compared to matched non-fracturing women, Bone 97 (2017) 233–242, 10.1016/j.bone.2017.01.031. [PubMed: 28132909]

[15]. Boskey AL, Donnelly E, Boskey E, Spevak L, Ma Y, Zhang W, Lappe J, Recker RR, Examining the relationships between bone tissue composition, compositional heterogeneity, and fragility fracture: A matched case-controlled FTIRI study, J. Bone Miner. Res 31 (2016) 1070–1081, 10.1002/jbmr.2759. [PubMed: 26636271]

[16]. Rizzo S, Farlay D, Akhter M, Boskey A, Recker R, Lappe J, Boivin G, Variables reflecting the mineralization of bone Tissue from fracturing versus nonfracturing postmenopausal nonosteoporotic women, JBMR Plus 2 (2018) 323–327, 10.1002/jbm4.10062. [PubMed: 30460335]

[17]. Morris MD, Mandair GS, Raman assessment of bone quality, Clin. Orthop. Relat. Res 469 (2011) 2160–2169, 10.1007/s11999-010-1692-y. [PubMed: 21116756]

[18]. Mandair GS, Morris MD, Contributions of Raman spectroscopy to the understanding of bone strength, Bonekey Rep. 4 (2015), 10.1038/bonekey.2014.115.

[19]. Yerramshetty JS, Lind C, Akkus O, The compositional and physicochemical homogeneity of male femoral cortex increases after the sixth decade, Bone 39 (2006) 1236–1243, 10.1016/j.bone.2006.06.002. [PubMed: 16860007]

[20]. Buckley K, Kerns JG, Vinton J, Gikas PD, Smith C, Parker AW, Matousek P, Goodship AE, Towards the in vivo prediction of fragility fractures with Raman spectroscopy, J. Raman Spectrosc 46 (2015) 610–618, 10.1002/jrs.4706. [PubMed: 27546955]

[21]. Demers JLH, Esmonde-White FWL, Esmonde-White KA, Morris MD, Pogue BW, Next-generation Raman tomography instrument for non-invasive in vivo bone imaging, Biomed. Opt. Express 6 (2015) 793–806, 10.1364/boe.6.000793. [PubMed: 25798304]

[22]. Kim G, Cole JH, Boskey AL, Baker SP, van der Meulen MCH, Reduced tissue-level stiffness and mineralization in osteoporotic cancellous bone, Calcif. Tissue Int 95 (2014) 125–131, 10.1007/s00223-014-9873-4. [PubMed: 24888692]

[23]. McCreadie BR, Morris MD, Chen TC, Rao DS, Finney WF, Widjaja E, Goldstein SA, Bone tissue compositional differences in women with and without osteoporotic fracture, Bone 39 (2006) 1190–1195, 10.1016/j.bone.2006.06.008. [PubMed: 16901772]

[24]. Gamsjaeger S, Buchinger B, Zwettler E, Recker R, Black D, Gasser JA, Eriksen EF, Klaushofer K, Paschalis EP, Bone material properties in actively bone-forming trabeculae in postmenopausal women with osteoporosis after three years of treatment with once-yearly Zoledronic acid, J. Bone Miner. Res 26 (2011) 12–18, 10.1002/jbmr.180. [PubMed: 20645415]

[25]. Hassler N, Gamsjaeger S, Hofstetter B, Brozek W, Klaushofer K, Paschalis E, Effects of long-term alendronate treatment on postmenopausal osteoporosis bone material properties, Osteoporos. Int 26 (2015) 339–352, 10.1007/s00198-014-2929-5. [PubMed: 25315260]

[26]. Beattie JR, Sophocleous A, Caraher MC, O'Driscoll O, Cummins NM, Bell SEJ, Towler M, Yazdi AR, Ralston SH, Idris AI, Raman spectroscopy as a predictive tool for monitoring osteoporosis therapy in a rat model of postmenopausal osteoporosis, J. Mater. Sci. Mater. Med 30 (2019), 10.1007/s10856-019-6226-x.

[27]. Monzem S, Sonego DA, Martini AD, Moura A, da Silva FG, de Faria JLB, de Souza RL, Raman spectroscopic of osteoporosis model in mouse tibia in vivo, Vib. Spectrosc 98 (2018) 88–91, 10.1016/j.vibspec.2018.07.013.

[28]. Shah FA, Stoica A, Cardemil C, Palmquist A, Multiscale characterization of cortical bone composition, microstructure, and nanomechanical properties in experimentally induced osteoporosis, J. Biomed. Mater. Res. A 106 (2018) 997–1007, 10.1002/jbm.a.36294. [PubMed: 29143443]

[29]. Orkoula MG, Vardaki MZ, Kontoyannis CG, Study of bone matrix changes induced by osteoporosis in rat tibia using Raman spectroscopy, Vib. Spectrosc 63 (2012) 404–408, 10.1016/j.vibspec.2012.09.016.

[30]. Awonusi A, Morris MD, Tecklenburg MMJ, Carbonate assignment and calibration in the raman spectrum of apatite, Calcif. Tissue Int 81 (2007) 46–52, 10.1007/s00223-007-9034-0. [PubMed: 17551767]

[31]. Falgayrac G, Facq S, Leroy G, Cortet B, Penel G, New method for Raman investigation of the orientation of collagen fibrils and crystallites in the Haversian system of bone, Appl. Spectrosc 64 (2010) 775–780, 10.1366/000370210791666255. [PubMed: 20615291]

[32]. Mandair GS, Steenhuis P, Ignelzi MA, Morris MD, Bone quality assessment of osteogenic cell cultures by Raman microscopy, J. Raman Spectrosc 50 (2019) 360–370, 10.1002/jrs.5521.

[33]. Olejnik C, Falgayrac G, During A, Cortet B, Penel G, Doses effects of zoledronic acid on mineral apatite and collagen quality of newly-formed bone in the rat's calvaria defect, Bone 89 (2016) 32–39, 10.1016/j.bone.2016.05.002. [PubMed: 27168397]

[34]. Buckley K, Matousek P, Parker AW, Goodship AE, Raman spectroscopy reveals differences in collagen secondary structure which relate to the levels of mineralisation in bones that have evolved for different functions, J. Raman Spectrosc 43 (2012) 1237–1243, 10.1002/jrs.4038.

[35]. Burke MV, Atkins A, Akens M, Willett TL, Whyne CM, Osteolytic and mixed cancer metastasis modulates collagen and mineral parameters within rat vertebral bone matrix, J. Orthop. Res 34 (2016) 2126–2136, 10.1002/jor.23248. [PubMed: 27027407]

[36]. Unal M, Uppuganti S, Leverant CJ, Creecy A, Granke M, Voziyan P, Nyman JS, Assessing glycation-mediated changes in human cortical bone with Raman spectroscopy, J. Biophotonics 11 (2018), 10.1002/jbio.201700352.

[37]. Burr DB, Changes in bone matrix properties with aging, Bone 120 (2019) 85–93, 10.1016/j.bone.2018.10.010. [PubMed: 30315999]

[38]. Kourkoumelis N, Zhang XZ, Lin ZM, Wang J, Fourier transform infrared spectroscopy of bone tissue: Bone quality assessment in preclinical and clinical applications of osteoporosis and fragility fracture, Clin. Rev. Bone Miner. Metabol 17 (2019) 24–39, 10.1007/s12018-018-9255-y.

[39]. Unal M, Creecy A, Nyman JS, The role of matrix composition in the mechanical behavior of bone, Curr. Osteoporos. Rep 16 (2018) 205–215, 10.1007/s11914-018-0433-0. [PubMed: 29611037]

[40]. Akhter MP, Lappe JM, Davies KM, Recker RR, Transmenopausal changes in the trabecular bone structure, Bone 41 (2007) 111–116, 10.1016/j.bone.2007.03.019. [PubMed: 17499038]

[41]. Esmonde-White FWL, Esmonde-White KA, Morris MD, Minor distortions with major consequences: Correcting distortions in imaging spectrographs, Appl. Spectrosc 65 (2011) 85–98, 10.1366/10-06040. [PubMed: 21211158]

[42]. Rauch F, Travers R, Glorieux FH, Cellular activity on the seven surfaces of iliac bone: A histomorphometric study in children and adolescents, J. Bone Miner. Res 21 (2006) 513–519, 10.1359/jbmr.060108. [PubMed: 16598370]

[43]. Banerjee S, Li DY, Interpreting multicomponent infrared spectra by derivative minimization, Appl. Spectrosc 45 (1991) 1047–1049, 10.1366/0003702914336282.

[44]. Taylor EA, Lloyd AA, Salazar-Lara C, Donnelly E, Raman and Fourier Transform Infrared (FT-IR) Mineral to Matrix Ratios Correlate with Physical Chemical Properties of Model Compounds and Native Bone Tissue, 71 (2017) 2404–2410, 10.1177/0003702817709286.

[45]. Colard T, Falgayrac G, Bertrand B, Naji S, Devos O, Balsack C, Delannoy Y, Penel G, New insights on the composition and the structure of the acellular extrinsic fiber cementum by Raman analysis, PLoS One 11 (2016), e0167316, 10.1371/journal.pone.0167316.

[46]. Bonifacio A, Sergo V, Effects of sample orientation in Raman microspectroscopy of collagen fibers and their impact on the interpretation of the amide III band, Vib. Spectrosc 53 (2010) 314–317, 10.1016/j.vibspec.2010.04.004.

[47]. Suzuki M, Kato H, Wakumoto S, Vibrational analysis by Raman spectroscopy of the interface between dental adhesive resin and dentin, J. Dent. Res 70 (1991) 1092–1097, 10.1177/00220345910700071501. [PubMed: 2066492]

[48]. Li R, Verreault D, Payne A, Hitchcock CL, Povoski SP, Martin EW, Allen HC, Effects of laser excitation wavelength and optical mode on Raman spectra of human fresh colon, pancreas, and prostate tissues, J. Raman Spectrosc 45 (2014) 773–780, 10.1002/jrs.4540.

[49]. Nyman JS, Makowski AJ, Patil CA, Masui TP, O'Quinn EC, Bi XH, Guelcher SA, Nicollela DP, Mahadevan-Jansen A, Measuring Differences in Compositional Properties of Bone Tissue by Confocal Raman Spectroscopy, Calcif. Tissue Int 89 (2011) 111–122, 10.1007/s00223-011-9497-x. [PubMed: 21597909]

[50]. Long JP, Hollister SJ, Goldstein SA, A paradigm for the development and evaluation of novel implant topologies for bone fixation: In vivo evaluation, 45 (2012) 2651–2657, 10.1016/j.jbiomech.2012.08.011.

[51]. Chauhan S, Pradhan S, Mohanty R, Saini A, Devi K, Sahu MC, Evaluation of sensitivity and specificity of bone marrow trephine biopsy tests in an Indian teaching hospital, Alex. J. Med 54 (2018) 161–166, 10.1016/j.ajme.2017.04.003.

[52]. Ascenzi MG, Chin J, Lappe J, Recker R, Non-osteoporotic women with low-trauma fracture present altered birefringence in cortical bone, Bone 84 (2016) 104–112, 10.1016/j.bone.2015.10.010. [PubMed: 26514952]

[53]. Homminga J, Van-Rietbergen B, Lochmuller EM, Weinans H, Eckstein F, Huiskes R, The osteoporotic vertebral structure is well adapted to the loads of daily life, but not to infrequent "error" loads, Bone 34 (2004) 510–516, 10.1016/j.bone.2003.12.001. [PubMed: 15003798]

[54]. Homminga J, McCreadie BR, Ciarelli TE, Weinans H, Goldstein SA, Huiskes R, Cancellous bone mechanical properties from normals and patients with hip fractures differ on the structure level, not on the bone hard tissue level, Bone 30 (2002) 759–764, 10.1016/s8756-3282(02)00693-2. [PubMed: 11996916]

[55]. Kreider JM, Goldstein SA, Trabecular bone mechanical properties in patients with fragility fractures, Clin. Orthop. Relat. Res 467 (2009) 1955–1963, 10.1007/s11999-009-0751-8. [PubMed: 19247731]

[56]. Patel S, Tweed K, Chinappen U, Fall-related risk factors and osteoporosis in older women referred to an open access bone densitometry service, 34 (2005) 67–71, 10.1093/ageing/afh238.

[57]. Unal M, Yang S, Akkus O, Molecular spectroscopic identification of the water compartments in bone, Bone 67 (2014) 228–236, 10.1016/j.bone.2014.07.021. [PubMed: 25065717]

[58]. Kumar R, Gronhaug KM, Afseth NK, Isaksen V, Davies CD, Drogset JO, Lilledahl MB, Optical investigation of osteoarthritic human cartilage (ICRS grade) by confocal Raman spectroscopy: a pilot study, 407 (2015) 8067–8077, 10.1007/s00216-015-8979-5.

[59]. Takahashi Y, Sugano N, Takao M, Sakai T, Nishii T, Pezzotti G, Raman spectroscopy investigation of load-assisted microstructural alterations in human knee cartilage: Preliminary study into diagnostic potential for osteoarthritis, 31 (2014) 77–85, 10.1016/j.jmbbm.2013.02.014.

[60]. Dehring KA, Smukler AR, Roessler BJ, Morris MD, Correlating changes in collagen secondary structure with aging and defective type II collagen by Raman spectroscopy, 60 (2006) 366–372, 10.1366/000370206776593582.

[61]. Harris M, Cilwa K, Elster EA, Potter BK, Forsberg JA, Crane NJ, Pilot study for detection of early changes in tissue associated with heterotopic ossification: moving toward clinical use of Raman spectroscopy, 56 (2015) 144–152, 10.3109/03008207.2015.1013190.

[62]. Mandair GS, Steenhuis P, Ignelzi MA, Morris MD, Bone quality assessment of osteogenic cell cultures by Raman microscopy, 50 (2019) 360–370, 10.1002/jrs.5521.

[63]. Bigelow EMR, Patton DM, Mandair G, Ward FS, Schlecht SH, Morris MD, Kohn D, Bredbenner TL, Jepsen KJ, Age-related changes in bone strength of male radii depend on outer bone size, 33 (2018) 238–238,

[64]. Ko ACT, Choo-Smith LP, Hewko M, Leonardi L, Sowa MG, Dong CCS, Williams P, Cleghorn B, Ex vivo detection and characterization of early dental caries by optical coherence tomography and Raman spectroscopy, 10 (2005), 031118 10.1117/1.1915488.

[65]. Shiraishi A, Miyabe S, Nakano T, Umakoshi Y, Ito M, Mihara M, The combination therapy with alfacalcidol and risedronate improves the mechanical property in lumbar spine by affecting the material properties in an ovariectomized rat model of osteoporosis, 10 (2009), 66 10.1186/1471-2474-10-66.

[66]. Iwasaki Y, Kazama JJ, Yamato H, Matsugaki A, Nakano T, Fukagawa M, Altered material properties are responsible for bone fragility in rats with chronic kidney injury, 81 (2015) 247–254, 10.1016/j.bone.2015.07.015.

[67]. Sekita A, Matsugaki A, Nakano T, Disruption of collagen/apatite alignment impairs bone mechanical function in osteoblastic metastasis induced by prostate cancer, 97 (2017) 83–93, 10.1016/j.bone.2017.01.004.

[68]. Ascenzi MG, Liao VP, Lee BM, Billi F, Zhou H, Lindsay R, Cosman F, Nieves J, Bilezikian JP, Dempster DW, Parathyroid hormone treatment improves the cortical bone microstructure by improving the distribution of type I collagen in postmenopausal women with osteoporosis, 27 (2012) 702–712, 10.1002/jbmr.1497.

[69]. Stockhausen KE, Qwamizadeh M, Wölfel EM, Hemmatian H, Fiedler IAK, Flenner S, Longo E, Amling M, Greving I, Ritchie RO, Schmidt FN, Busse B, Collagen Fiber Orientation Is Coupled with Specific Nano-Compositional Patterns in Dark and Bright Osteons Modulating Their Biomechanical Properties, 15 (2021) 455–467, 10.1021/acsnano.0c04786.

[70]. Kakar S, Einhorn TA, Vora S, Miara LJ, Hon G, Wigner NA, Toben D, Jacobsen KA, Al-Sebaei MO, Song M, Trackman PC, Morgan EF, Gerstenfeld LC, Barnes GL, Enhanced chondrogenesis and Wnt signaling in PTH-treated fractures, 22 (2007) 1903–1912, 10.1359/jbmr.070724.

[71]. Hadjiargyrou M, Lombardo F, Zhao SC, Ahrens W, Joo J, Ahn H, Jurman M, White DW, Rubin CT, Transcriptional profiling of bone regeneration - Insight into the molecular complexity of wound repair, 277 (2002) 30177–30182, 10.1074/jbc.M203171200.

[72]. Macsai CE, Foster BK, Xian CJ, Poles of Wnt signalling in bone growth, remodelling, skeletal disorders and fracture repair, 215 (2008) 578–587, 10.1002/jcp.21342.

[73]. Milat F, Ng KW, Is Wnt signalling the final common pathway leading to bone formation?, 310 (2009) 52–62, 10.1016/j.mce.2009.06.002.

[74]. Makitie RE, Haanpaa M, Valta H, Pekkinen M, Laine CM, Lehesjoki AE, Schalin-Jantti C, Makitie O, Skeletal Characteristics of WNT1 Osteoporosis in Children and Young Adults, 31 (2016) 1734–1742, 10.1002/jbmr.2841.

[75]. Sturznickel J, Rolvien T, Delsmann A, Butscheidt S, Barvencik F, Mundlos S, Schinke T, Kornak U, Amling M, Oheim R, Clinical Phenotype and Relevance of LRP5 and LRP6 Variants in Patients With Early-Onset Osteoporosis (EOOP), 36 (2021) 271–282, 10.1002/jbmr.4197.

[76]. Albanese I, Yu B, Al-Kindi H, Barratt B, Ott L, Al-Refai M, de Varennes B, Shum-Tim D, Cerruti M, Gourgas O, Rheaume E, Tardif JC, Schwertani A, Role of Noncanonical Wnt Signaling Pathway in Human Aortic Valve Calcification, 37 (2017) 543-+, 10.1161/atvbaha.116.308394.

[77]. Zhou YH, Lin JY, Shao J, Zuo QL, Wang SF, Wolff A, Nguyen DT, Rintoul L, Du ZB, Gu YT, Peng YY, Ramshaw JAM, Long X, Xiao Y, Aberrant activation of Wnt signaling pathway altered osteocyte mineralization, 127 (2019) 324–333, 10.1016/j.bone.2019.06.027.

[78]. Beier EE, Maher JR, Sheu TJ, Cory-Slechta DA, Berger AJ, Zuscik MJ, Puzas JE, Heavy Metal Lead Exposure, Osteoporotic-like Phenotype in an Animal Model, and Depression of Wnt Signaling, 121 (2013) 97–104, 10.1289/ehp.1205374.

[79]. Zaugg LK, Banu A, Walther AR, Chandrasekaran D, Babb RC, Salzlechner C, Hedegaard MAB, Gentleman E, Sharpe PT, Translation Approach for Dentine Regeneration Using GSK-3 Antagonists, J. Dent. Res 99 (2020) 544–551, 0022034520908593 10.1177/0022034520908593. [PubMed: 32156176]

[80]. Ferreira VCD, Lopes AP, Alves NM, Sousa FRN, Pereira KMA, Gondim DV, Girao VCC, Leitao RFC, Goes P, Bisphosphonate-related osteonecrosis induced change in alveolar bone architecture in rats with participation of Wnt signaling, Clin. Oral Investig 25 (2021) 673–682, 10.1007/s00784-02-003551-7.

[81]. Cesar R, Leivas TP, Pereira CAM, Boffa RS, Guarniero R, Reiff R.B.d.M., Netto A. Mandeli, Fortulan CA, Rollo J.M.D.d.A., Axial compressive strength of human vertebrae trabecular bones classified as normal, osteopenic and osteoporotic by quantitative ultrasonometry of calcaneus, Res. Biomed. Eng 33 (2017) 91–96, 10.1590/2446-4740.04116

[82]. Cesar R, Boffa RS, Fachine LT, Leivas TP, Silva AMH, Pereira CAM, Reiff RBM, Rollo JMDA, Evaluation of trabecular microarchitecture of normal osteoporotic and osteopenic human vertebrae, Procedia Eng. 59 (2013) 6–15, 10.1016/j.proeng.2013.05.087.

[83]. Kazakia GJ, Burghardt AJ, Link TM, Majumdar S, Variations in morphological and biomechanical indices at the distal radius in subjects with identical BMD, J. Biomech 44 (2011) 257–266, 10.1016/j.jbiomech.2010.10.010. [PubMed: 21071031]

[84]. Freeman JJ, Wopenka B, Silva MJ, Pasteris JD, Raman spectroscopic detection of changes in bioapatite in mouse femora as a function of age and in vitro fluoride treatment, Calcif. Tissue Int 68 (2001) 156–162, 10.1007/s002230001206. [PubMed: 11351499]

[85]. McElderry JDP, Zhao GS, Khmaladze A, Wilson CG, Franceschi RT, Morris MD, Tracking circadian rhythms of bone mineral deposition in murine calvarial organ cultures, J. Bone Miner. Res 28 (2013) 1846–1854, 10.1002/jbmr.1924. [PubMed: 23505073]

[86]. Miller LM, Little W, Schirmer A, Sheik F, Busa B, Judex S, Accretion of bone quantity and quality in the developing mouse skeleton, J. Bone Miner. Res 22 (2007) 1037–1045, 10.1359/jbmr.070402. [PubMed: 17402847]

[87]. Gamsjaeger S, Hofstetter B, Fratzl-Zelman N, Roschger P, Roschger A, Fratzl P, Brozek W, Masic A, Misof BM, Glorieux FH, Klaushofer K, Rauch F, Paschalis EP, Pediatric reference Raman data for material characteristics of iliac trabecular bone, Bone 69 (2014) 89–97, 10.1016/j.bone.2014.09.012. [PubMed: 25245203]

[88]. Roschger A, Gamsjaeger S, Hofstetter B, Masic A, Blouin S, Messmer P, Berzlanovich A, Paschalis EP, Roschger P, Klaushofer K, Fratzl P, Relationship between the v(2)PO(4)/amide III ratio assessed by Raman spectroscopy and the calcium content measured by quantitative backscattered electron microscopy in healthy human osteonal bone, J. Biomed. Opt 19 (2014), 10.1117/1.jbo.19.6.065002.

[89]. Shi C, Mandair GS, Zhang HH, Vanrenterghem GG, Ridella R, Takahashi A, Zhang YS, Kohn DH, Morris MD, Mishina Y, Sun HC, Bone morphogenetic protein signaling through ACVR1 and BMPR1A negatively regulates bone mass along with alterations in bone composition, J. Struct. Biol 201 (2018) 237–246, 10.1016/j.jsb.2017.11.010. [PubMed: 29175363]

[90]. Karampas IA, Orkoula MG, Kontoyannis CG, A quantitative bioapatite/collagen calibration method using Raman spectroscopy of bone, J. Biophotonics 6 (2013) 573–586, 10.1002/jbio.201200053. [PubMed: 22961694]

[91]. Kazanci M, Roschger P, Paschalis EP, Klaushofer K, Fratzl P, Bone osteonal tissues by Raman spectral mapping: Orientation-composition, J. Struct. Biol 156 (2006) 489–496, 10.1016/j.jsb.2006.06.011. [PubMed: 16931054]

[92]. Rokidi S, Paschalis EP, Klaushofer K, Vennin S, Desyatova A, Turner JA, Watson P, Lappe J, Akhter MP, Recker RR, Organic matrix quality discriminates between age- and BMD-matched fracturing versus non-fracturing post-menopausal women: A pilot study, Bone 127 (2019) 207–214, 10.1016/j.bone.2019.06.017. [PubMed: 31229674]

[93]. Osipov B, Emami AJ, Christiansen BA, Systemic Bone Loss After Fracture, 16 (2018) 116–130, 10.1007/s12018-018-9253-0.

[94]. Emami AJ, Toupadakis CA, Telek SM, Fyhrie DP, Yellowley CE, Christiansen BA, Age Dependence of Systemic Bone Loss and Recovery Following Femur Fracture in Mice, 34 (2019) 157–170, 10.1002/jbmr.3579.

[95]. Eastell R, Robins SP, Colwell T, Assiri AMA, Riggs BL, Russell RGG, Evaluation of bone turnover in type I osteoporosis using biochemical markers specific for both bone formation and bone resorption, Osteoporos. Int. 3 (1993) 255–260, 10.1007/bf01623829.

[96]. Rai M, Rai T, D'sa J, Rai S, Bone turnover markers: An emerging tool to detect primary osteoporosis, J. Clin. Diag. Res 12 (2018), 10.7860/jcdr/2018/37917.12389.

[97]. Burnell JM, Baylink DJ, Chestnut CH, Mathews MW, Teubner EJ, Bone matrix and mineral abnormalities in postmenopausal osteoporosis, Metabolism 31 (1982) 1113–1120, 10.1016/0026-0495(82)90161-5. [PubMed: 7132738]

[98]. Willett TL, Pasquale J, Grynpas MD, Collagen modifications in postmenopausal osteoporosis: Advanced glycation endproducts may affect bone volume, structure and quality, Curr. Osteoporos. Rep 12 (2014) 329–337, 10.1007/s11914-014-0214-3. [PubMed: 24880722]

[99]. Paschalis EP, Gamsjaeger S, Dempster D, Jorgetti V, Borba V, Boguszewski CL, Klaushofer K, Moreira CA, Fragility fracture incidence in chronic obstructive pulmonary disease (COPD) patients associates with nanoporosity, mineral/matrix ratio, and pyridinoline content at actively

bone-forming trabecular surfaces, J. Bone Miner. Res 32 (2017) 165–171, 10.1002/jbmr.2933. [PubMed: 27490957]

[100]. Paschalis EP, Gamsjaeger S, Fratzl-Zelman N, Roschger P, Masic A, Brozek W, Hassler N, Glorieux FH, Rauch F, Klaushofer K, Fratzl P, Evidence for a Role for Nanoporosity and Pyridinoline Content in Human Mild Osteogenesis Imperfecta, J. Bone Miner. Res 31 (2016) 1050–1059, 10.1002/jbmr.2780. [PubMed: 26748579]

[101]. Kopp J, Bonnet M, Renou JP, Effect of collagen crosslinking on collagen-water interactions (a DSC investigation), Matrix 9 (1990) 443–450, 10.1016/s0934-8832(11)80013-2.

[102]. Dong XN, Qin A, Xu J, Wang X, In situ accumulation of advanced glycation endproducts (AGEs) in bone matrix and its correlation with osteoclastic bone resorption, Bone 49 (2011) 174–183, 10.1016/j.bone.2011.04.009. [PubMed: 21530698]

[103]. Yeni YN, Yerramshetty J, Akkus O, Pechey C, Les CM, Effect of fixation and embedding on Raman spectroscopic analysis of bone tissue, 78 (2006) 363–371, 10.1007/s00223-005-0301-7.

[104]. Unal M, Jung H, Akkus O, Novel Raman Spectroscopic Biomarkers Indicate That Postyield Damage Denatures Bone's Collagen, 31 (2016) 1015–1025, 10.1002/jbmr.2768.

[105]. Rauch F, Travers R, Norman ME, Taylor A, Parfitt AM, Glorieux FH, The bone formation defect in idiopathic juvenile osteoporosis is surface-specific, 31 (2002) 85–89, Pii s8756–3282(02)00814–1 10.1016/s8756-3282(02)00814-1.

[106]. Du JY, Flanagan CD, Bensusan JS, Knusel KD, Akkus O, Rimnac CM, Raman biomarkers are associated with cyclic fatigue life of human allograft cortical bone, J. Bone Joint Surg. Am 101 (2019), 10.2106/jbjs.18.00832.

Highlights

- A case-control evaluation of Raman spectroscopic measures of bone quality was performed in osteopenic women with and without low-trauma fractures.
- Aggregate univariate case-control and logistic regression analyses show that the organization of mineralized collagen fibrils was significantly altered in cortical cases compared to controls.
- Bone compositional and heterogeneity parameters related to mineral/matrix ratios, B-type carbonate substitution, and mineral crystallinity were not significantly different between cases and controls.
- This is the first blinded prospective-controlled study to show that Raman spectroscopy can differentiate fractures cases from controls.

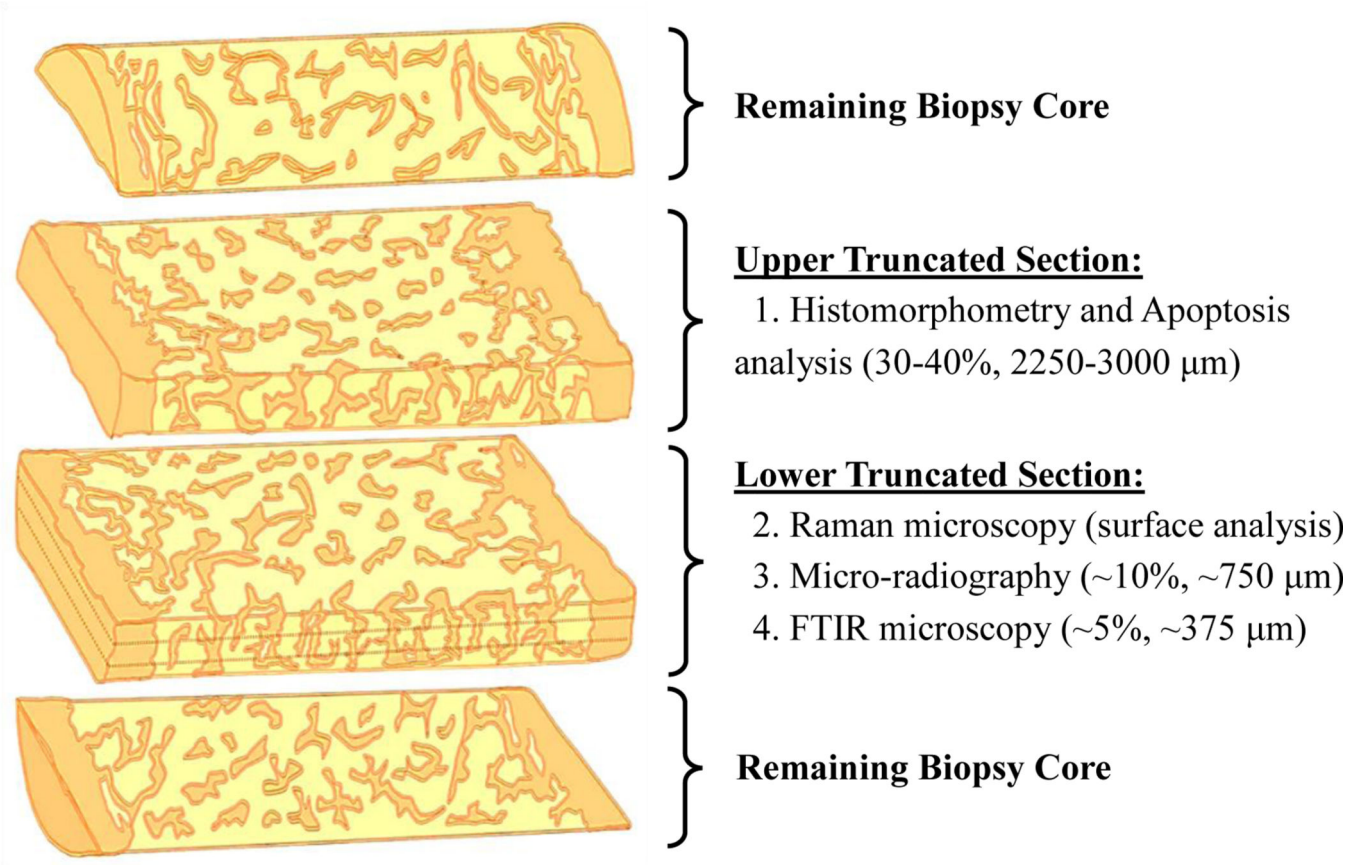

Figure 1.

Schematic of embedded cylindrical biopsy allocation and analysis. The surface of the lower truncated section was analyzed by Raman microscopy (this study) prior to resectioning for microradiography (Rizzo *et al*) and FTIR (Boskey *et al*) analysis. A second biopsy core was also acquired from the same study participant for nano-indentation testing (Vennin *et al*).

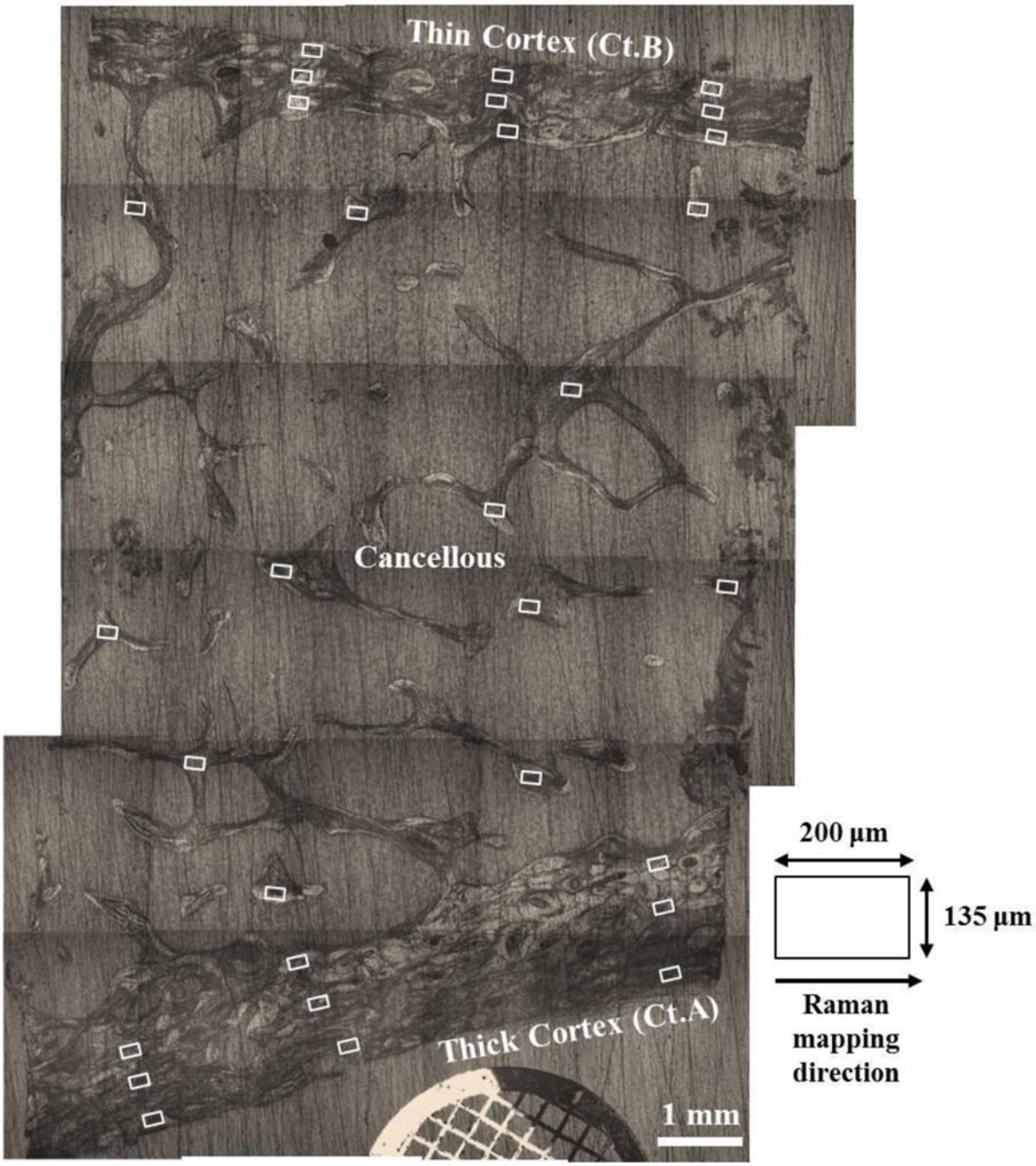

Figure 2.

Reconstructed longitudinal image of an iliac crest biopsy section showing the approximate surface locations of all 18 cortical and 12 cancellous Raman maps (white boxes). The laser line is ~135 µm in length and is aligned perpendicularly to the thick cortex (Ct.A) and the thin cortex (Ct.B) prior to Raman mapping.

Table 1.

Subject characteristics (mean ± S.D.).Cases vs. controls.

Subject Characteristics	**Controls (*n*=59)**	**Cases (*n*=59)**	***p*** [a]
Age (years)	61.7 ± 7.3	62.0 ± 7.5	0.38
BMD of hip (g/cm^3)	0.823 ± 0.072	0.827 ± 0.083	0.57
BMD of hip T-score	−0.978 ± 0.586	0.947 ±0.678	0.59
Low trauma fractures (*n*)			
Wrist	0	20	
Ankle	0	15	
Humerus	0	7	
Patella	0	4	
Shoulder	0	3	
Elbow	0	2	
Hip	0	2	
Other: *fibula, foot, knee, lower leg, pelvis, and wrist & elbow combined.*	0	6	
Vertebral	0	23	

[a]Case-control statistical comparisons performed using the Wilcoxon Signed Rank.

Abbreviations: S.D., standard deviation.

Table 2.

Subject characteristics and Raman parameter data (mean ± SDs). Cases vs. controls.

		Controls (*n*=59)	Cases (*n*=59)	*p*[a]
Cortical Bone				
Mineral/Matrix	ν_1PO_4/Amide I	8.76 ± 0.78	8.93 ± 0.96	0.24
	ν_1PO_4/Pro+Hyp	17.88 ± 1.18	17.80 ± 1.17	0.60
	ν_1PO_4/Pro	11.02 ± 0.59	10.96 ± 0.66	0.54
	ν_1PO_4//Phe	16.63 ± 1.77	16.46 ± 1.68	0.44
Crystallinity (cm^{-1})	FWHM (ν_1PO_4)[b]	16.42 ± 0.21	16.43 ± 0.20	0.72
Carbonate/Phosphate	Carb/ν_1PO_4	0.232 ± 0.006	0.233 ± 0.007	0.64
Carbonate/Matrix	Carb/Phe	3.858 ± 0.396	3.835 ± 0.417	0.66
Organization	1248/1268	1.054 ± 0.025	1.043 ± 0.022	**0.0061**
	1044/959	0.141 ± 0.006	0.143 ± 0.005	**0.0242**
Collagen	Hyp/Pro[b]	0.582 ± 0.033	0.592 ± 0.046	*0.0956*
	Phe/(Pro+Hyp)[b]	0.495 ± 0.053	0.505 ± 0.069	0.50
Polymer infiltration	MMA/(Pro+Hyp)[b]	0.072 ± 0.024	0.071 ± 0.023	0.93
Cancellous Bone				
Mineral/Matrix	ν_1PO_4/Amide I	8.72 ± 0.66	8.93 ± 0.88	0.15
	ν_1PO_4/Pro+Hyp	19.28 ± 1.82	19.17 ± 1.68	0.81
	ν_1PO_4/Pro	11.43 ± 0.92	11.46 ± 0.88	0.63
	ν_1PO_4//Phe	15.58 ± 2.25	15.41 ± 2.27	0.91
Crystallinity (cm^{-1})	FWHM (ν_1PO_4)[b]	16.35 ± 0.24	16.38 ± 0.23	0.56
Carbonate/Phosphate	Carb/ν_1PO_4	0.235 ± 0.006	0.235. ± 0.007	0.80
Carbonate/Matrix	Carb/Phe	3.629 ± 0.501	3.603. ± 0.496	0.90
Organization	1248/1268	1.045 ± 0.026	1.036 ± 0.025	**0.0154**
	1044/959	0.139 ± 0.007	0.141 ± 0.006	*0.0661*
Collagen	Hyp/Pro[b]	0.577 ± 0.021	0.582 ± 0.025	0.42
	Phe/(Pro+Hyp)[b]	0.555 ± 0.066	0.561 ± 0.078	0.60
Polymer infiltration	MMA/(Pro+Hyp)[b]	0.080 ± 0.028	0.077 ± 0.027	0.65

Abbreviations: S.D., standard deviation.

[a]Comparisons based on Wilcoxon signed rank test (significant *p* values are in **bold** and borderline significant *p* values are in *italics*).

[b]Values obtained from Gaussian-fitted Raman spectra.

Table 3.

Sample Variance of Raman parameters (mean ± SDs). Cases vs. controls

		Controls (*n*=59)	Cases (*n*=59)	*p*[a]
Cortical Bone				
Mineral/Matrix	ν_1PO_4/Amide I	0.845 ± 0.620	0.974 ± 0.714	0.38
	ν_1PO_4/Pro+Hyp	2.601 ± 1.633	2.950 ± 2.037	0.31
	ν_1PO_4/Pro	0.903 ± 0.472	0.962 ± 0.521	0.46
	ν_1PO_4//Phe	6.544 ± 3.277	6.870 ± 3.069	0.61
Crystallinity (cm^{-1})	FWHM (ν_1PO_4)[b]	0.021 ± 0.010	0.020 ± 0.012	0.45
Carbonate/Phosphate	Carb/ν_1PO_4	0.043 ± 0.022[c]	0.051 ± 0.027 [c]	0.22
Carbonate/Matrix	Carb/Phe	0.318 ± 0.176	0.315 ± 0.148	0.95
Organization	1248/1268	0.343 ± 0.289[c]	0.338 ± 0.305[c]	0.63
	1044/959	0.064± 0.031[c]	0.073 ± 0.048[c]	0.42
Collagen	Hyp/Pro[b]	1.137 ± 1.577[c]	1.954 ± 4.100[c]	**0.0302**
	Phe/(Pro+Hyp)[b]	0.0102 ± 0.0172	0.0097 ± 0.0127	0.60
Polymer infiltration	MMA/(Pro+Hyp)[b]	0.365 ± 0.277[c]	0.329 ± 0.258[c]	0.53
Cancellous Bone				
Mineral/Matrix	ν_1PO_4/Amide I	0.911 ± 0.480	0.839 ± 0.444	0.50
	ν_1PO_4/Pro+Hyp	3.818 ± 2.290	3.640 ± 2.332	0.79
	ν_1PO_4/Pro	1.041 ± 0.475	1.068 ± 0.521	0.89
	ν_1PO_4//Phe	6.701 ± 2.702	6.467 ± 3.009	0.73
Crystallinity (cm^{-1})	FWHM (ν_1PO_4)[b]	0.024 ± 0.11	0.025 ± 0.14	0.64
Carbonate/Phosphate	Carb/ν_1PO_4	0.084 ± 0.037[c]	0.090 ± 0.045[c]	0.46
Carbonate/Matrix	Carb/Phe	0.312 ± 0.151	0.321 ± 0.170	0.82
Organization	1248/1268	1.098 ± 1.159[c]	0.957 ± 0.739[c]	0.97
	1044/959	0.101 ± 0.052[c]	0.115 ± 0.063[c]	0.20
Collagen	Hyp/Pro[b]	0.959 ± 0.924[c]	1.113 ± 1.251[c]	0.90
	Phe/(Pro+Hyp)[b]	0.0090 ± 0.0110	0.0141 ± 0.0229	0.11
Polymer infiltration	MMA/(Pro+Hyp)[b]	0.320 ± 0.243[c]	0.261 ± 0.207[c]	*0.0709*

Abbreviations: S.D., standard deviation.

[a] Comparisons based on Wilcoxon signed rank test (significant *p* values are in **bold** and borderline significant *p* values are in *italics*).

[b] Values obtained from Gaussian-fitted Raman spectra.

[c] Divide values by a factor of x1000.

Table 4.

Heterogeneity data of Raman parameters (mean ± SDs). Cases vs. controls.

		Controls (*n*=59)	Cases (*n*=59)	*p*[a]
Cortical Bone				
Mineral/Matrix	ν_1PO_4/Amide I	2.772 ± 0.457	2.843 ± 0.443	0.34
	ν_1PO_4/Pro+Hyp	5.867 ± 0.956	5.924 ± 0.865	0.98
	ν_1PO_4/Pro	3.939 ± 0.475	4.064 ± 0.491	0.37
	ν_1PO_4//Phe	8.691 ± 1.343	8.663 ± 1.120	0.75
Carbonate/Phosphate	Carb/ν_1PO_4	0.043 ± 0.005	0.044 ± 0.005	0.38
Carbonate/Matrix	Carb/Phe	1.971 ± 0.262	1.974 ± 0.272	0.99
Organization	1248/1268	0.352 ± 0.039	0.350 ± 0.049	0.58
	1044/959	0.0405 ± 0.0048	0.0411 ± 0.0055	0.65
Cancellous Bone				
Mineral/Matrix	ν_1PO_4/Amide I	3.019 ± 0.424	3.051 ± 0.416	0.38
	ν_1PO_4/Pro+Hyp	7.518 ± 1.394	7.259 ± 1.282	0.22
	ν_1PO_4/Pro	4.672 ± 0.658	4.753 ± 0.791	0.94
	ν_1PO_4//Phe	8.559 ± 1.444	8.402 ± 1.475	0.58
Carbonate/Phosphate	Carb/ν_1PO_4	0.048 ± 0.005	0.048 ± 0.006	0.99
Carbonate/Matrix	Carb/Phe	1.986 ± 0.358	1.917 ± 0.319	0.43
Organization	1248/1268	0.394 ± 0.042	0.383 ± 0.049	0.28
	1044/959	0.0455 ± 0.0047	0.0457 ± 0.0056	0.69

Abbreviations: S.D., standard deviation. Comparisons based on Wilcoxon signed rank test. Heterogeneity data based on the full-width height (FWHM) of Raman map histograms.

Table 5.

Reduced Logistic Regression Models and Odds Ratio (OR) Estimates Predicting Past Low-Trauma Fractures in Osteopenic Women.

Model	Action	Explanatory Parameters	OR	95% CI	*p*-value
1A	Reduced model after elimination of non- explanatory parameters	Ct. 1248/1268 ratio	0.617	0.406–0.938	0.024
1B	Reduced model after elimination of non- explanatory parameters	Ct. 1044/959 ratio	1.656	1.083–2.534	0.020
2A	Add age and BMD[#] to Model-1A	Ct. 1248/1268 ratio, Age, and BMD	0.620	0.405–0.947	0.027
2B	Add age and BMD[#] to Model-1B	Ct. 1044/959 ratio, Age, and BMD	1.697	1.095–2.632	0.018

Data expressed as Odds Ratio (OR) and corresponding 95% Confidence Intervals (CI).

[#]Bone Mineral Density (BMD) of the hip (g/cm^3).

Table 6.

Summary of false positives and negatives, sensitivity, and specificity in osteopenic postmenopausal women with low-trauma fractures.

Model	Explanatory Parameters	TP (*n*)	TN (*n*)	FP (*n*)	FN (*n*)	*Sensitivity (%)*	*Specificity (%)*
1A	Ct. 1248/1268 ratio	38	30	21	29	64.4	50.8
1B	Ct. 1044/959 ratio	35	29	24	30	59.3	49.2
2A	Ct. 1248/1268 ratio, Age, and BMD	38	31	21	28	64.4	52.5
2B	Ct. 1044/959 ratio, Age, and BMD	37	29	22	30	62.7	49.2

Abbreviations: TP = True Positive, TN = True Negative, FP = False Positive, FN = False Negatives, Sensitivity = TP/(TP + FN) × 100%; and Specificity = TN/(FP + TN) × 100%.